

*Final Report to the Air Force Office of Scientific Research, February, 2005, Grant Number  
F49620-02-1-0087*

## **Low Dimensional Methods for Jet Noise Control**

Charles E. Tinney\* and Mark N. Glauser<sup>†</sup>  
*Syracuse University, Syracuse, NY, 13244, U.S.A.*

Lawrence S. Ukeiley<sup>‡</sup>  
*University of Mississippi, University, MS, 38677, U.S.A.*

**DISTRIBUTION STATEMENT A**  
Approved for Public Release  
Distribution Unlimited

20050519 090

---

\*Ph.D. Candidate, Dept. of Mech. & Aerospace. Eng., 151 Link Hall.

<sup>†</sup>Professor, Dept. of Mech. & Aerospace. Eng., 151 Link Hall.

<sup>‡</sup>Senior Research Scientist, National Center for Physical Acoustics.

Low dimensional techniques are applied to the compressible turbulent mixing layer in the sound source regions of the flow from a cold (75°F) Mach 0.85 jet ( $z/D=3$  to 8) using POD and Fourier decomposition. Measurements are acquired along the streamwise cross plane ( $r, \theta$ ) using a multi-component PIV system with an azimuthal grid spacing of  $10^\circ$  to prevent aliasing of the Fourier-azimuthal modes. The decomposition is performed using single, two and three component forms of the POD ( $u$ -streamwise,  $v$ -radial,  $w$ -azimuthal) applied in radius. Fourier decomposition is applied along the azimuthal direction because of the mean periodic nature of axisymmetric flows. The relative distribution of energy from these low-dimensional techniques is shown to be consistent with Glauser & George<sup>5</sup> and Jung *et al.*<sup>8</sup> who used the scalar ( $u$ ) form in the incompressible axisymmetric mixing layer, and Ukeiley *et al.*<sup>18</sup> who used a vector form (streamwise and radial component) in the compressible Mach 0.30 & 0.60 axisymmetric jet. The dominant Fourier-azimuthal modes in the current investigation at  $z/D=3$  and  $z/D=8$  are  $m = 5$  and  $m = 2$ , respectively. These are similar to the previous findings whereby the mean energy shifts to lower modes with the growth of the mixing layer.

Using the findings from this low-dimensional analysis, a Modified form of Bonnet *et al.*'s<sup>2</sup> Complementary Technique is employed to reconstruct temporally, the evolution of the decomposition technique's expansion coefficients via Adrian's<sup>1</sup> Linear Stochastic Estimation. This employs an azimuthal array of fifteen dynamic pressure transducers as the unconditional grid. These transducers are located outside of the turbulent sound source regions of the flow, so that the acoustical characteristics of the sound source events are not disturbed. From this low-dimensional estimate, a volcano like event, similar the one modelled by Glauser & George,<sup>5</sup> and later shown (experimentally) by Citrinit & George<sup>3</sup> has been revealed. It is this event that is thought to produce much of the noise experienced in the far field acoustic regions.

A survey of the far field noise was performed simultaneously with the near field pressure. The final stages of the technique (to be performed in the future) will compare an estimate of the far field noise (using the low-dimensional reconstruction of the velocity field extracted in this study) to the actual far field survey in order to identify the characteristic event(s) that are responsible for most of the sources of noise in these complex flows.

## I. Introduction

The noise due to current military and commercial jet aircraft engines continues to be a major environmental concern both ashore and afloat. In general, the noise is created by the turbulent mixing of a high speed (high temperature) jet exhaust plume with the ambient air, thus creating massive pressure fluctuations in the near field and ultimately large acoustic signatures in the acoustic far field regions of the flow. These acoustic signatures have been recognized as potential sources of physical and environmental hazards to air crew, ground support personnel, as well as those residing and working in the vicinity of the active aviation operations, because of their high frequency and high intensity noise characteristics. Within recent years, federal programs in the United States have been developed for

improving the acoustical compactness of real estate surrounding our country's airports and air bases including programs targeted for land acquisition. In particular the Federal Aviation Administration (FAA) through the Airport Improvement Program (AIP) has spent over \$2.7 billion, or 11.5 percent of available AIP grants, for noise related projects since 1982, of which \$1.6 billion was spent between 1992 and 1999. While other government centers, (NASA, DoD) have been coordinating programs aimed at source identification and reduction, the exact nature of these sound sources has yet to be fully understood. The current research effort has focused on the latter aspect of source identification for eventual control and reduction.

While there exists a number of experimental and numerical techniques in the research community (i.e., Large Eddy Simulation, Direct Numerical Simulation of the Navier-Stokes Equations, Wavelet analysis, Cross Spectral Analysis, Causality Methods, Low-Dimensional and Complementary Techniques), each of which is capable of contributing new findings to this complex problem, it is important to understand the characteristic strengths and weaknesses of these techniques in the context of establishing a reliable scientific approach for understanding these highly dynamic sources of noise.

In the experimental community, the classical limitations have most notably been the intrusive nature of the experimental instrumentation, and their inability to preserve the natural acoustic characteristics from these sources. Where optics based tools, Laser Doppler Velocimetry (LDV), Particle Image Velocimetry (PIV), Time Resolved Particle Image Velocimetry (TRPIV) have proven to be effectively less intrusive in capturing the sound sources, they too have their limitations (i.e., LDV can only perform single-point measurements, PIV and even TRPIV have too low a sampling rate [up to 4kHz at best] to resolve the highly dynamic sound mechanisms [substantial energy is found even beyond 20kHz]). In addition, these techniques by themselves only provide planar information whereas the methods used here provide a volume of the flow field allowing for the computation of the necessary derivatives.

## II. Noise and the Jet

With the advent of thermodynamic propulsion systems in the early 1950's, "sound generated aerodynamically" has since remained a problem with the rapidly increasing use of these systems. After the second World War, a necessity for understanding the sources of noise from these systems was clear. The seminal work of Sir James Lighthill (<sup>49</sup>) has become the bases for interpreting the complex nature of these noise related problems. Although the original formulations have been refined, the theory remains central. Of particular notice is Lighthill's famous eighth-power law (equation 1) which immediately impacted the design and development of the high bypass-ratio aircraft engines.

$$I \propto \rho_0 \frac{U^8}{a_\infty^5} \left(\frac{L}{R}\right)^2 \quad (1)$$

where  $I$  is the radiated sound intensity,  $\rho$  is the gas density,  $a_\infty$  is the sound speed of the ambient (still) air,  $U$  and  $L$  are the velocities and correlation length scales of the energy containing eddies, and  $R$  is the distance from the source.

Lighthill's original model approach reformulated the compressible equations of motion into a form for the propagation of acoustic waves.

$$\frac{\partial^2 \rho}{\partial t^2} - a_\infty^2 \rho = \frac{\partial^2 T_{ij}}{\partial x_i \partial x_j} \quad (2)$$

where the terms on the left-hand side represent the acoustic wave propagation, and the terms on the right are the sources of sound. This inhomogeneous wave equation employs Lighthill's famous stress tensor:

$$T_{ij} = \rho u_i u_j + (p - \rho a_\infty^2) \delta_{ij} - \tau_{ij} \quad (3)$$

Some advances in recent years have simplified expression 3. Powell<sup>56</sup> determined that for mildly heated jets  $p - \rho a_\infty^2 = 0$ , and Creighton<sup>32</sup> showed that jet noise was primarily an inviscid process. Thus, the only contributing term left in equation 3 is the Reynolds stress term  $\rho u_i u_j$ , and the sound pressure in the far field at a distance  $x$  from the sound region is then reduce to a point source quadrupole.

$$p'(x, t) = \int_V \frac{\partial^2 T_{ij}}{\partial x_i \partial x_j} \left( y, t - \frac{|x - y|}{a_\infty} \right) \frac{dy}{4\pi|x - y|} \quad (4)$$

where  $V$  is the volume of fluid generating the noise,  $x$  and  $y$  are the locations of the observation point and fluid volume respectively and  $t - \frac{|x - y|}{a_\infty}$  is the retarded time. The solutions to Lighthill's wave equation and additions to the theory are discussed in many places such as Goldstein<sup>39</sup> or Lilley.<sup>50</sup>

The source terms are second partial derivatives and are referred to as quadrupoles. In recent years, Ukeiley<sup>19</sup> studied the time dependence of these quadrupole source terms in the Mach 0.85 axisymmetric jet using a single rake of hot-wire probes so that no azimuthal variation was obtained. The rake employed six radially spaced probes and was traversed between 4 and 12 jet diameters downstream of the exit plane. The noise sources were determined from a formulation of Lighthill's acoustic analogy presented in Avital *et al.*<sup>25</sup> This analysis assumed no variation in azimuth so that the contribution from the lateral quadrupoles were zero in the compact limit. In terms of instantaneous events there is no reason for this assumption to be valid, however, with the existing data set this assumption had to be made and it was felt that insight into the structure of the turbulent sources could still be gained. From their formulation the acoustic power output distribution, as a function of streamwise location, was written as;

$$P(x, t) = \alpha_{ij} \ddot{Q}_{ii} \int \ddot{q}_{jj} d\xi, \quad (5)$$

where

$$\ddot{Q}_{11} = 2\pi \frac{\partial^2}{\partial t^2} \int \int u^2 r dr dx, \quad (6)$$

$$\ddot{Q}_{22} = \pi \frac{\partial^2}{\partial t^2} \int \int v^2 r dr dx, \quad (7)$$

$$\ddot{q}_{11} = 2\pi \frac{\partial^2}{\partial t^2} \int u^2 r dr \quad (8)$$

$$\ddot{q}_{22} = \pi \frac{\partial^2}{\partial t^2} \int v^2 r dr, \quad (9)$$

In the above equations  $\ddot{q}_{11}$  and  $\ddot{q}_{22}$  are thought of as time dependent quadrupoles or source terms. Because Constant Temperature Anemometry (CTA) tools were employed in the investigation (and are sensitive to density variations), velocity ( $u$ ) was replaced with mass flux ( $\rho u$ ), although it was shown that the density fluctuations were relatively small.

Many other novel approaches have been undertaken to identify: the sources of noise, the resultant radiated noise, and the physics associated with the sound generation process from high speed jets. Recently Freund,<sup>36</sup> investigated the noise sources in low a Reynolds number, axisymmetric, Mach 0.9, turbulent jet by direct numerical simulation. Using Lighthill's theory to determine the normal sources of noise and a numerical solution of Lighthill's equation to compare the computational procedures, he found that the phase velocities of the sources contributed significantly to the noise. These were found to convect at approximately 5% to 50% of the ambient sound speed.

### A. Identifying Turbulent Structures

The importance of large scale structures in turbulent flows has been known for quite some time. The dynamics of these structures have been shown to control many of the events that characterize turbulence, and has been a topic of some debate as scientists interpret their physical makeup.

Lumley<sup>9</sup> suggested a quantitative technique for identifying the more energetic structures in turbulent flows. The analysis requires that an optimization of a random field be represented by a set of deterministic functions which are in turn functions of the field itself. The early work of Glauser & George<sup>38</sup> utilized this decomposition technique in the turbulent shear layer of the incompressible axisymmetric jet and showed that the dominant basis function (1<sup>st</sup> POD mode) contained 40% of the total *TKE*, with an additional 40% of the energy found in the next two modes. An extension of this study by Citriniti & George<sup>3</sup> and Gamard & George<sup>37</sup> captured the temporal evolution of the jet's  $r, \theta$  plane using a highly dense grid of 138 single-wire probes (Reynolds number of  $8e^5$ ). This later investigation used the POD to filter out small-scale fluctuations, capable of obscuring the large-scale interactions in the turbulent shear layer. Ukeiley *et al.*<sup>18</sup> and Taylor *et al.*<sup>14</sup> performed similar studies of the  $r, \theta$  plane in the turbulent sound source regions of the Mach 0.3 & 0.6 compressible axisymmetric jet. They concluded that the dominant POD mode converged rapidly and contained over 40% of the fluctuating mean square mass flux. This was performed at 4 and 8 diameters downstream from the jet lip. Further measurements were conducted at  $M = 0.85$ , although because of high probe breakage, the decomposition technique could not be applied to the higher Mach number flow. Comparisons were made, and similarities found, in the spectral measurements at all Mach numbers (0.3, 0.6 & 0.85) suggesting similarity in the POD solution at  $M = 0.85$ .

Other successful applications of this technique to transitional and turbulent flows have been performed, [e.g.<sup>54, 4, 3, 14, 37</sup> Delville *et al.*,<sup>33, 6440</sup> and Glauser *et al.*<sup>6</sup>]. For more detail of the POD's mathematical construction, its historical applications to turbulent flows, as

well as its relation to other modelling techniques, i.e. Galerkin projection, Linear Stochastic Estimation, pattern recognition, and others, the reader is referred to<sup>28</sup> and Glauser & George.<sup>5</sup> The use of these low-dimensional techniques, have added a wealth of knowledge to understanding the interactive nature of turbulent shear flows.

## B. Seiner's "Rational" Approach on Jet Noise

In an attempt to combine the aforementioned techniques, Seiner<sup>13</sup> proposes that jet noise control schemes may be based upon a low-dimensional description of the turbulent flow field. He posits that such low-dimensional descriptions can be generated by applying the Proper Orthogonal Decomposition (POD) technique to the correlations of turbulent two-point statistics. Seiner asserts that from such low-dimensional descriptions, Lighthill's<sup>48,49</sup> acoustic analogy approach to understanding aerodynamically generated sound may be used to determine which low-order turbulent spatial structures are responsible for noise generation, thus providing the base state for the design of control methodologies.

The resultant physics that have been shown from these low-dimensional tools, clearly depicts the existence of a candidate structure for the noise generation: a high strain, short duration event that has been identified repeatedly in the near field jet shear layer via these experimental low dimensional tools, [Glauser & George,<sup>4</sup> Citriniti & George,<sup>3</sup> Jung *et al.*,<sup>8</sup> Gamard *et al.*,<sup>37</sup> Gordyev & Thomas<sup>40</sup>]. By utilizing such tools in conjunction with a simultaneous sampling of the acoustic field, it can be determined whether this event and/or others is/are responsible for most of the far field noise. It should be made clear that the goal is not to develop predictive schemes for radiated noise, as is the typical application of Lighthill's analogy or much of the work performed by Tam<sup>60</sup> and his co-workers, but to identify the noise producing events which can then be altered through control. It should also be added that the importance of these large coherent structures and their role in the generation of noise has had some historical findings including the work of: Juve *et al.*,<sup>47</sup> Ffowcs Williams & Kempton,<sup>35</sup> Seiner,<sup>13</sup> Freund,<sup>36</sup> Tam,<sup>60</sup> and Bastin *et al.*<sup>27</sup>

Many of the experimental techniques for studying coherent structures and the low-dimensional picture they provide are dependent on the utilization of multi-point techniques, as they are capable of resolving the spatial character of a flow's turbulent structure(s). These include conditional sampling, pseudo flow visualization, Linear Stochastic Estimation (LSE), and the Proper Orthogonal Decomposition (POD). To appreciate the need for these one must understand the character of high Reynolds number, often turbulent, motions. As modern full Navier-Stokes computer simulations have made clear, knowing the data at many points in the flow does little in and of itself to make clear what is happening because of the chaotic nature of the flow. The key to understanding usually lies in what is done to the data to bring the underlying order to the foreground.

With these low-dimensional tools in mind, Seiner<sup>13</sup> proposes a rational approach whereby the double divergence of a single two-point velocity correlation, which is derived from a simplified version of the Lighthill stress tensor, can be written as:

$$\frac{\partial(u_i u_j)}{\partial x_i} = -\varepsilon_{ijk} u_j \omega_k + \frac{1}{2} \frac{\partial(u_i u_j)}{\partial x_i}. \quad (10)$$

The first term on the right hand side is Lamb's vector and the second one is the dynamic

pressure. Taking the divergence of the above equation yields;

$$\frac{\partial^2(u_i u_j)}{\partial x_i \partial x_j} = -\varepsilon_{ijk}(S_{ij}\omega_k + r_{ij}\omega_k) \quad (11)$$

where  $S_{ij}$  is the strain rate tensor and  $r_{ij}$  is the rotation rate tensor. To arrive at equation 11 the double divergence is taken of the two-point correlation in a similar manner to taking the double divergence of the Greens function as is classically done in solving for Lighthill's stress tensor, Tam.<sup>60</sup> Since the strain rate is representative of a force being applied to a gas and the rotation rate being its response, then the phase difference between them is due to the finite time required for the gas to respond. Seiner postulated that it is possible for the phase difference to be an indicator of noise producing events. From the data sets available in this research effort, the time histories of both the strain and rotation rate tensors of the low-dimensional velocity field can be created. These will be examined with the simultaneously sampled far field acoustic time histories to identify if the noise producing events coincide with increases in this phase lag. If this is the case, then minimizing the phase lag may represent a tractable goal in a noise control scheme.

### III. Objectives

The principle objective of this research has been to identify the noise producing events in the compressible turbulent shear layer of a Mach 0.85, 2inch diameter, axisymmetric, cold ( $104^\circ F$ ) jet that are responsible for the far field acoustic noise. The unique character of this experiment utilized a non-intrusive technique by implementing lip pressure measurements to estimate several downstream velocity planes ( $r, \theta$  plane) while simultaneously sampling the far field acoustics. The modal dominance was found from the decomposition of the velocity field using the Proper Orthogonal Decomposition (in radius) and Fourier decomposition (in azimuth) Techniques. With a modified form of the Complementary Technique, the low-dimensional structures in the velocity field are reconstructed from the fluctuating lip pressure alone, thus revealing the large-scale turbulent events that are believed to be responsible for the much of the far field acoustic energy.

The key to the success of this research is the simultaneous knowledge of the low dimensional velocity field and the far field noise. The work to date has involved multiple rakes of hot-wire anemometry probes capable of capturing the spectral content of the velocity field and producing multi-point statistics. By coupling these measurements with the Complementary technique, a low dimensional picture of the jet's unsteady turbulent shear layer has been illustrated, thus revealing a high strain, short duration event. It is thought that this event is responsible for the generation of noise from the large scale motions of the flow, Taylor *et al.*<sup>14</sup> However, the hot-wire methods are intrusive and, by their very presence, have a strong influence on the far field noise.

With that said, the current investigation has been able to overcome these experimental limitations using modified Complementary Techniques. The advantages to this stems from a less intrusive arrangement of instruments that are coupled with these low dimensional analytical tools, which have been proven effective in illustrating the large scale motions of this flow. The implementation of this technique to the current facility is described as follows.

The velocity field is captured about the  $r, \theta$  plane at several streamwise locations using stereo Particle Image Velocimetry (PIV), capable of resolving 3 components of velocity.

From this extensive database, the characteristic two point correlations of the velocity field are generated, as is needed for performing the decomposition technique. Thus the velocity field has been reduced to its dominant low-dimensional structures in order to provide a clear picture of the noise producing events. The PIV tool is unable to capture the temporal evolution of this flow. With this in mind, an azimuthal array of fifteen pressure transducers, strategically placed at the lip of the jet, were sampled simultaneously with the velocity field (via PIV), and the far field acoustics. Because the pressure transducers have the bandwidth and resolution necessary for resolving the flow field's dynamics, a first order estimation technique, Adrian,<sup>1</sup> is utilized to estimate a low-dimensional picture of the velocity field from the unsteady pressure at the lip.

The velocity field estimation is based on an estimation coefficient generated from the two-point correlation of the POD random coefficients and the fluctuating pressure field, and the pressure field itself. This technique of using a Modified Complementary technique was proven recently with the work of Taylor *et al.*<sup>14</sup> for flow over a back word facing ramp subject to unsteady pressure gradient where the flow was estimated from the wall pressure, and Schmit (2002) where the trailing vortex from a micro air vehicle was estimated from strain sensors located on the surface of the wing.

The importance of utilizing a modified version of the Complementary Technique is to remove the intrusive nature of classical instruments, such as CTA, used to capture the velocity field while trying to resolve the far field acoustics. Thus a direct examination of the far field acoustics with the near field velocity can be obtained without disturbing the acoustic characteristics of the near field noise spectrum.

## IV. Low Dimensional Tools

### A. Proper Orthogonal Decomposition

Lumley's Proper Orthogonal Decomposition has been shown to be an effective technique for decomposing a stationary random field of vectors into a characteristic basis set, from which the maximization of the ordered basis defines the most probable vector from that set, in the mean square sense. This maximization relies on selecting a candidate event with the largest mean square projection on the vector field  $\vec{u}$  (via the calculus of variations), and the normalization follows from  $|\alpha|^2 = |\vec{u}, \phi|^2 / |\phi, \phi^*|$ . This leads to the integral eigenvalue problem(12).

$$\int \int R_{ij}(\vec{x}, \vec{x}') \phi_j(\vec{x}') d\vec{x}' = \lambda \phi_i(\vec{x}) \quad (12)$$

Here the kernel  $R_{ij}$  is the velocity (ensemble averaged) two-point cross-correlation tensor created from a series of discrete stationary turbulent flow events,  $R_{ij}(\vec{x}, \vec{x}') = \langle u_i(\vec{x}, t) u_j(\vec{x}', t) \rangle$ , and the eigenvalue  $\lambda$  is equal to  $|\alpha|^2$ . The technique is optimized in that most of the energy is contained in the first structure alone. Some of the more general mathematical properties are outlined as follows.

1. The kernel is positive definite and is a function of the flow field:

$$0 < \sum_{i,j=1}^n R_{ij} x_i y_j \quad (13)$$

2. The orthonormal sequence of eigenfunctions  $\phi^{(n)}$  for the discrete set  $n = 1, 2, 3, \dots$  obeys the law of the Kronecker delta function  $\delta_{p,q}$ :

$$\int_D \phi_i^{(p)}(\vec{x}) \phi_i^{(q)}(\vec{x}) d\vec{x} = \delta_{p,q} \quad (14)$$

3. The eigenvalues and eigenfunctions, being properties of the kernel, can be utilized to reconstruct the original kernel:

$$R_{ij}(\vec{x}, \vec{x}') = \sum_{n=1}^{\infty} \lambda^{(n)} \phi_i^{(n)}(\vec{x}) \phi_j^{(n)}(\vec{x}') \quad (15)$$

4. The orthonormal sequence is ordered:

$$\lambda^{(1)} > \lambda^{(2)} > \lambda^{(3)} \dots > 0 \quad (16)$$

5. The eigenfunctions can be used to reconstruct the original generalized ensemble:

$$u_i(\vec{x}, t) = \sum_{n=1}^{\infty} a_n(t) \phi_i^{(n)}(\vec{x}) \quad (17)$$

with

$$a_n(t) = \int_D u_i(\vec{x}, t) \phi_i^{(n)}(\vec{x}) d\vec{x} \quad (18)$$

6. The random coefficients  $a_n$  are uncorrelated, and are equal to the eigenvalues:

$$\langle a_n a_m \rangle = \lambda^{(n)} \delta_{n,m} \quad (19)$$

An appealing characteristic of this axisymmetric flow, is that the azimuthal direction is periodic and symmetric, in the mean square sense. Hence the eigenfunctions are harmonic in this direction and the POD can be simplified by performing the Fourier transform about the azimuthal plane. This simplification is commonly applied to systems that are stationary, homogenous or periodic, the latter being the condition for this experiment. Also, the azimuthal correlation satisfies the even function relation, thus the new kernel,  $B_{ij}$  is constructed from the Fourier cosine transformation of the original cross-correlation function  $R_{ij}$ .

$$R_{ij}(r, r', \Delta\theta, z_o) = \sum_{m=0}^{\infty} B_{ij}(r, r', m, z_o) \cos m\theta \quad (20)$$

where for  $m = 0$ ,

$$B_{ij}(r, r', 0, z_o) = \frac{1}{\pi} \int_0^\pi R_{ij}(r, r', \Delta\theta, z_o) d\theta. \quad (21)$$

and for  $m > 0$  otherwise,

$$B_{ij}(r, r', m, z_o) = \frac{2}{\pi} \int_0^\pi R_{ij}(r, r', \Delta\theta, z_o) \cos m\theta d\theta. \quad (22)$$

Here  $z_o$  is used to designate a particular streamwise position, and  $\Delta\theta$  as the azimuthal separation between  $\theta_o$  and  $\theta'$ . The transformation to a Fourier azimuthal mode number,  $m$ , using (21) and (22) results in an altered form of (12),

$$\int_D B_{ij}(r, r', m, z_o) \phi_j^{(n)}(r', m, z_o) r' dr' = \lambda^{(n)}(m, z_o) \phi_i^{(n)}(r, m, z_o) \quad (23)$$

If the random field is stationary in time, the kernel can be constructed using the averaged spectral signatures of the stationary measurements. As already pointed out, the flow through the axisymmetric jet is invariant in  $\theta$ . Thus if we choose to replace the time averaged kernel with a ensemble averaged spectral tensor (this can be obtained by using multiple rakes of CTA, capable of resolving adequate bandwidths unlike PIV) the problem's solution becomes capable of displaying the spectral character of the candidate structures.

Under these conditions a spectral tensor can be defined by

$$B_{ij}(r, r', z_o, m, f) = \int R_{ij}(r, r', z_o, \Delta\theta, \tau) e^{i(2\pi f\tau + m\Delta\theta)} d\tau d\theta, \quad (24)$$

and  $B_{ij}$  becomes the kernel in the integral eigenvalue problem:

$$\begin{aligned} \int \int B_{ij}(r, r', z_o, m, f) \phi_j^n(r', m, f, z_o) r' dr' \\ = \lambda^n(m, f) \phi_i^n(r, m, f, z_o), \end{aligned} \quad (25)$$

where the eigenfunctions are now  $\phi_j^n(r, m, f, z_o)$ . In (24) and (25),  $f$  is the temporal frequency in Hz. It should be noted that in this case the eigenvalues and eigenfunctions are now functions of temporal frequency  $f$ , as well as streamwise location and azimuthal mode number  $m$ . A summary of the solutions to this problem can be found in Ukeiley *et al.*<sup>18</sup> for the high Mach number subsonic jet.

## B. Linear Stochastic Estimation

In 1977, Adrian<sup>1</sup> proposed that stochastic estimation could be applied to unconditional correlation data. This method uses what Adrian has termed a "conditional eddy." This term is used to denote vector fields given by the conditional average  $\hat{\mathbf{u}}(\mathbf{x}', t) = \langle \mathbf{u}(\mathbf{x}', t) | \mathbf{u}(\mathbf{x}, t) \rangle$ . This formulation implies that the velocity fluctuation at position  $\mathbf{x}'$  can be estimated knowing the velocity fluctuation at position  $\mathbf{x}$  at the same instant. Furthermore, the conditional average is the best estimate, in the mean square sense, of  $\mathbf{u}(\mathbf{x}', t)$  in terms of  $\mathbf{u}(\mathbf{x}, t)$  (v. Tung and Adrian<sup>62</sup>). Stochastic estimation uses the conditional information specified about the flow at one or more locations in conjunction with its statistical properties to infer a typical behavior at the remaining locations. The conditional eddy can be estimated using various quantities as the condition.

Cole *et al.*<sup>31</sup> utilized the instantaneous velocities collected with a rake of cross-wire probes as the condition in a plane of an axisymmetric jet. They found this afforded many possible probe combinations for estimating the simultaneous velocity vector field at one or more points across the span. Furthermore, they discuss what number of probes and their

respective positions are the most appropriate to obtain the best estimate of the velocity field in this plane of the axisymmetric jet.

This technique involves expanding the conditional average in a Taylor series about  $\mathbf{u}(\mathbf{x}, t) = 0$  and truncating the series after the first order terms. This procedure yields the following estimate for  $\hat{\mathbf{u}}(\mathbf{x}', t)$ ,

$$\tilde{u}_i(\mathbf{x}', t) = A_{ij}(\mathbf{x}')u_j(\mathbf{x}, t). \quad (26)$$

Values for the estimation coefficients,  $A_{ij}(\mathbf{x}')$ , are chosen such that the mean square error is minimized as  $e_i = \langle [\tilde{u}_i(\mathbf{x}', t) - \langle u_i(\mathbf{x}', t) | u(\mathbf{x}, t) \rangle]^2 \rangle$  for  $i = 1, 2, 3$ . This minimization requires that  $\frac{\partial e_i}{\partial A_{ij}(\mathbf{x}')} = 0$  which leads to an equation of the form

$$\overline{u_j(\mathbf{x})u_k(\mathbf{x})}A_{ik}(\mathbf{x}') = \overline{u_j(\mathbf{x})u_i(\mathbf{x}')} \quad (27)$$

where  $\overline{u_j(\mathbf{x})u_k(\mathbf{x})}$  and  $\overline{u_j(\mathbf{x})u_i(\mathbf{x}')}$  are the Reynolds stress and two-point correlation tensor, respectively. It should be noted that for the system of equations, (27), only the two-point velocity correlation data is utilized. These systems **are not** a function of the condition being investigated. The estimated velocity components are found from the expansion of (26). It is in these equations that the condition selected plays a role.

### C. Complementary Technique

In order to perform the projection required to obtain the time dependent expansion coefficients from the POD, (18), it is necessary to have knowledge of the flow field at all points in space simultaneously. From an experimental point of view this requires that the flow domain be measured simultaneously on a sufficient spatial grid so as to minimize the effects of spatial aliasing as discussed by Glauser and George.<sup>5</sup> This is extremely difficult and can require hundreds of hot wire probes, or full field measurement techniques which are currently limited to sampling rates insufficient for use in high Reynolds number flow. Refer to Citriniti<sup>3</sup> and Gamard *et al.*<sup>37</sup> for a study involving the simultaneous sampling of 138 single wire probes. The spatial two-point velocity correlation tensor on the other hand can be obtained on a sufficient spatial grid with as few as two hot wire probes. Here we briefly describe a technique which uses the spatially resolved statistical quantity, the two-point correlation tensor, in conjunction with the instantaneous information at only a few select points, to obtain estimates of the time dependent expansion coefficients.

This method is described in detail in Bonnet *et al.*<sup>2</sup> and is composed of four main steps.

1. The eigenfunctions and eigenvalues are obtained from direct application of the POD to the two-point tensor obtained on a sufficiently resolved spatial grid.
2. The Linear Stochastic Estimation (LSE) is applied to the cross-correlation tensor and multi-point estimates of the random vector field are computed as described by Cole *et al.*<sup>31</sup>
3. The estimated velocity field obtained from step two is projected onto the eigenfunctions obtained from step one to obtain the estimated expansion coefficients, i.e., the estimated velocity is used instead of the actual velocity in (18).

4. The estimated expansion coefficients from (18) are then used in conjunction with the POD eigenfunctions to reconstruct an estimate of the velocity field.

#### D. Modified Complementary Technique

By reformulating and combining the one-dimensional *LSE* with the *POD* it can be shown that the time-resolved instantaneous fluctuating pressure can be used to estimate the *POD* expansion coefficients as are necessary for computing an estimate of the low dimensional velocity field.

This reformulating replaces the velocity correlation terms in the *LSE* technique with a correlation created from the *POD* expansion coefficient and the instantaneous pressure using the same approach described in § B. Thus, in the modified complementary technique, the instantaneous fluctuating pressure (the fluctuating hydrodynamic pressure at the lip of the jet's nozzle) is used to determine the presence of the chosen conditional structure. This can be written symbolically as:

$$\tilde{a}_n(t; t) = \langle a_n(t) | p(t) \rangle \quad (28)$$

where  $\tilde{a}_n$  is the *POD* expansion coefficient that describes the velocity field over  $\vec{x}$ , given the instantaneous pressure,  $p(t)$ .

Just as with the traditional formulation of the *LSE*, the estimated *POD* coefficient can be written as a series expansion with each additional term containing increasing powers of the pressure condition.

$$\tilde{a}_n(t; t) = b_{ni}p_i(t) + c_{nij}p_i(t)p_j(t) + d_{nij}p_i(t)p_j(t)p_k(t) + \dots \quad (29)$$

Equation 29 can be truncated to include just the linear term plus the error associated with neglecting the higher order terms.

$$\tilde{a}_n(t) = b_{ni}p_i(t) + O[p_i^2(t)] \quad (30)$$

For the linearized modified *LSE*, the elements of  $b_{ni}$  are selected to minimize the mean square error,  $e_{\tilde{a}_n} = [\tilde{a}_n(t) - a_n(t)]^2$  by requiring  $\frac{\partial e_{\tilde{a}_n}}{\partial b_{ni}} = \frac{\partial [b_{ni}p_i(t) - a_n(t)]^2}{\partial b_{ni}} = 0$ . The solution to this minimization problem is a linear system of equations,  $\overline{p_j(t)p_k(t)b_{nk}} = \overline{a_n(t)p_j(t)}$ , which can be written in matrix form as:

$$\begin{bmatrix} \overline{p_1^2} & \overline{p_1p_2} & \cdots & \overline{p_1p_k} \\ \overline{p_2p_1} & \overline{p_2^2} & \cdots & \overline{p_2p_k} \\ \vdots & \vdots & \ddots & \vdots \\ \overline{p_jp_1} & \overline{p_jp_2} & \cdots & \overline{p_jp_k} \end{bmatrix} \begin{bmatrix} b_{n1} \\ b_{n2} \\ \vdots \\ b_{nk} \end{bmatrix} = \begin{bmatrix} \overline{a_np_1} \\ \overline{a_np_2} \\ \vdots \\ \overline{a_np_j} \end{bmatrix} \quad (31)$$

After solving equation 31 for the modified *LSE* coefficients, equation 30 can be used to compute the instantaneous *POD* coefficients from time-resolved pressure measurements. These can then be combined with the *POD* eigenfunctions to realize the velocity field. In summary, the steps involved in the modified complementary technique are:

- The original 2-D eigenvalue problem is created from the weighted kernel, (utilizes all nine of the 2 point velocity correlations). This requires a grid transformation from

the cartesian system (PIV vector maps are acquired in the cartesian system) to a cylindrical system in order to obtain the azimuthal modes.

$$\int_D B_{i,j}(r, r', m, z_o) \phi_j^{(n)}(r', m, z_o) r' dr' = \lambda^{(n)}(m, z_o) \phi_i^{(n)}(r, m, z_o) \quad (32)$$

- The random coefficients are calculated from the POD eigenfunctions at several independent time steps,  $(t_s)$ .

$$a_n(m, z_o, t_s) = \int_D u_i(r, r', m, z_o, t_s) \phi_i^{(n)}(r, m, z_o) dr \quad (33)$$

- From the simultaneous sampling of 15 kulite pressure transducers (distributed about the lip of the jet) with the stereo PIV system at the discrete time steps  $(t_s)$ , the *POD* random coefficients are correlated with instantaneous fluctuating lip pressure in order to determine the first order *LSE* estimation coefficients  $(b_{ni}(m, z_o))$ . The correlation between the lip pressure and the velocity field may include a phasing coefficient  $\alpha$ , based on the flow's mean convection velocity.

$$\overline{p_j(t_s - \alpha) p_k(t_s - \alpha) b_{nk}(m, z_o)} = \overline{a_n(m, z_o, t_s) p_j(t_s - \alpha)} \quad (34)$$

- From the *LSE* estimation coefficient, the random *POD* coefficients are estimated through the following expansion where the time function  $(t)$  is continuous because of the bandwidth and sampling capabilities of the pressure instruments.

$$\tilde{a}_n^{est}(m, z_o, t) = b_{nk}(m, z_o) p_j(t + \alpha) \quad (35)$$

- The low dimensional reconstruction of all points in the flow can now be performed by expanding the estimated random coefficients as follows,

$$u_i^{est}(r, r', m, z_o, t) = \sum_{n=1}^{\infty} a_n^{est}(m, z_o, t) \phi_i^{(n)}(r, m, z_o) \quad (36)$$

- The last step requires that the  $u_i^{est}(r, r', m, z_o, t)$  be transformed from the Fourier domain (azimuthal modes) to the spatial domain, (azimuthal structures).

The estimated velocity field from the modified complementary technique represents one of most complete data sets of a high Reynolds number compressible jet. Since the lip pressure and the far field acoustics are measured simultaneously we are able to examine the velocity and the radiated noise simultaneously without disturbing the far field noise spectrum.

## V. Design and Verification of an Anechoic Chamber for the Experimental Study of High Speed Heated Jets

### A. Introduction

The refurbishment of the  $7,300\text{ ft}^3$  ( $206\text{ m}^3$ ) anechoic chamber located at Syracuse University for studying aero-acoustically generated noise will now be discussed. The purpose of the facility is to provide free field conditions necessary for performing the current experimental effort. The facility has been updated with intentions of performing future jet studies at elevated temperatures near  $1000^\circ\text{F}$  ( $540^\circ\text{C}$ ). Safety issues are discussed because of the elevated temperatures, as well as concerns for ensuring acoustic quality. Several far field acoustic measurements will be acquired (in addition to the current research effort) over a range of Mach numbers and facility conditions in order to quantify the acoustic performance of the facility.

### B. Facility Design and Overview

The large anechoic chamber located at Syracuse University was originally constructed under the leadership of Dosanjh<sup>34</sup> (1972-1976) to study the effects of varying exit temperature and mass flow of secondary and tertiary annular jets surrounding a sonic, axisymmetric heated jet. Many of the measurements were acquired using a few far field (more than 80 diameters) acoustic microphones and shadow-graphic flow visualization techniques. Research studies continued in the early 1990's with studies pertaining to the control of impinging high speed jet resonance by Sheplak.<sup>59</sup> With these latter studies, the facility had primarily remained unchanged except for the replacement of the original compressor with a 100hp, 500psi. (3,450kPa.) power plant.

### C. Anechoic Chamber

The interior chamber dimensions including sound treatment (wedge tip to wedge tip) are 26ft. x 20ft. x 14ft. (8m. x 6m. x 4.3m.) with exterior walls, flooring and ceiling constructed from reinforced 12in. (30.5cm.) thick single poured concrete. All interior surfaces of the chamber are acoustically treated using fibreglass wedges with a cut off frequency of 150Hz. Wedge fabrication comprises of an interior high-density fibreglass wedge covered with lower-density fibreglass matting. The eductor duct and 6 pressure balancing ducts (to be described later on) are all treated with several layers of medium-density fiberglass held in place by perforated (46% solidity) metal sheeting. This was necessary to reduce any noise emitting from a centrifugal eductor fan and any outside sound disturbances such as passing aircraft and grounds crew equipment.

### D. Processed Airflow

The power plant that supplies air to the experimental jet rig is broken down as follows. Compressed air is supplied by a two stage (2 piston) Joy compressor at a maximum discharge of  $4.5\text{ ft}^3\text{ s}^{-1}$  ( $0.127\text{ m}^3\text{ s}^{-1}$ ), and 500psi. (3,450kPa.). The compressor discharges to a single bypass after-cooler and desiccant dryer capable of reducing the compressed air to a recommended  $-40^\circ\text{F}$  ( $-40^\circ\text{C}$ ) dew point. Five tanks with a volumetric capacity of  $1100\text{ ft}^3$

( $335m^3$ ) store the compressed air to a maximum pressure based on the performance of the compressor. The tanks also function as a plenum for the compressor, as not to experience piston cycling in the experimental jet rig. Also, the interiors of the tanks are lined to prevent corrosion. Refer to figure 11 for a process and instrumentation diagram of the compressed air system in the Syracuse University aero-acoustics research laboratory.

An electronically actuated control valve with a whisper trim interior is installed downstream of the tank storage and controls the flow to the experimental rig located in the chamber. The experimental jet rig is connected to the control valve via 150ft. (45.7m.) of 4in. (10.2cm.) inner diameter carbon steel piping followed by 60ft. (18m.) of 6in. inner diameter (15.2cm) stainless steel 304 *sch* - 40 wall piping. The junction between the smaller and larger diameter pipes is through a centrifugal filter / muffler and is necessary both for removing any debris emanating from the carbon steel pipe, and for reducing internal noise induced by the compressor and valve.

For purposes of running experimental studies at elevated temperatures, the facility is equipped with a 470kW Chromalox electric circulation heater shown in figure 12. The heater consists of 72 incoloy-800 sheathed rods that turn on and off, as needed, to achieve the desired output temperature. The output temperature is measured by an ungrounded thermocouple located in the flow stream before the experimental rig. The heater's construction and electrical input requirements were designed using a flow rate of  $21ft^3s^{-1}$  ( $0.59m^3/s$ ) and a nozzle exit temperature of  $1000^\circ F$  ( $540^\circ C$ ). Because of the difference in the discharge rate between the experimental rig and the compressor (over  $14ft^3s^{-1}$  or  $0.4m^3s^{-1}$ ), the facility is employed as a blow down system, as is the primary function of the large air storage mentioned earlier. The operational time of the jet rig when discharging at a rate of  $21ft^3s^{-1}$  (Mach 0.85 for a 2in. nozzle) yields a 25-minute window.

### E. Chamber Eductor and Bypass Air

The chamber eductor (exhaust) and eductor fan mentioned earlier consists of a belt driven centrifugal fan capable of discharging air at a constant rate of  $166.7ft^3s^{-1}$  ( $4.7m^3s^{-1}$ ). The additional source of air supply needed to balance the pressure deficit induced by the eductor fan is provided by the installation of an industrial variable Make-Up Air (MUA) unit capable of supplying  $116.7ft^3s^{-1}$  to  $233.3ft^3s^{-1}$ , ( $3.3m^3s^{-1}$  to  $6.6m^3s^{-1}$ ) of air at an exit temperature of 60F degrees, (33.3C deg.) above the temperature at the inlet. This MUA unit consists of a fan controlled by a variable frequency drive (VFD) that heats outside air as it is drawn through an 85% filter, to a desirable temperature through the firing of a gas burner. The treated air is then ducted into a large plenum located behind the back wall of the anechoic chamber with dimensions 13ft. x 10ft. x 22ft., (4m. x 3m. x 7m.).

The treated air travels from the plenum to the chamber through an axisymmetric 15ft. (4.6m.) acoustically treated duct with a 43in. (110cm.) interior diameter. The duct contains several mesh grid inserts and honeycomb for preventing large eddies from entering into the chamber. Also the duct that connects the plenum to the chamber is centered on the same axis of the jet rig, thus acting as the jet rig bypass air. This is done at speeds several orders of magnitude smaller than the jet rig exhaust speed. This bypass will also be crucial when operating the experimental jet rig at elevated temperatures, thus preventing the chamber from heating up and exposing any instrumentation to temperature conditions detrimental to their performance and reliability.

## F. Experimental Jet Rig

The experimental jet rig located in the anechoic chamber was designed with intentions of using optics based measurement tools (PIV) for capturing the velocity profiles of the jet's turbulent shear layer. Therefore the jet rig design consisted of two arrays of seeder injection ports necessary for PIV measurements. The first array is utilized for cold experiments and uses an olive oil seed (for any temperatures that may provide consistency in particle size, phase state and light scattering), whereas the second array for heated experiments uses a metallic based solution.

The interior profile of the jet rig is entirely axisymmetric and comprises of two custom machined members constructed entirely of 304 Stainless Steel. A custom flange houses a honeycomb flow straightening ceramic substrate and joins the two members. The substrate has a density of 400 cells per square inch and is capable of operating in temperatures of up to 2600° F (1450° C) with minimal growth. The pressure drop through a 3.2in. (8.13cm.) substrate (over half the diameter of the pipe) at  $21\text{ ft}^3\text{s}^{-1}$  is negligible at 0.53psi. (3.65kPa). With fear of eroding the ceramic substrate, the 6 metallic seeding injection ports are located downstream from the substrate and has been found to have little effect on the quality of the acoustics and the flow.

The jet nozzle's interior profile utilizes a matched 5th order polynomial contraction with a ratio of 3:1, for a 2in. (5.08cm.) exit diameter, and screws onto the experimental rig for capability of interchanging different nozzles in the future. The surface roughness of the experimental rig including the jet nozzle end piece is of order  $30\mu\text{m}$ . The nozzle's contraction shape was based on a ratio of length to steepness. For a contraction that is too steep, the flow experiences separation at the exit of the contraction, whereas a contraction that is too gradual experiences unwanted growth in the boundary layer. A compromise was found between the two phenomena. A scaled schematic of the nozzle profile and seeder characteristics is shown in figure 13.

The entire experimental jet rig is mounted to a stand designed to allow the jet and piping to grow naturally at elevated temperatures, (figure 14). The piping is 24ft. (8m.) in length and is constructed using the same stainless steel piping mentioned earlier. This was recommended for purposes of reducing internal noise generated by an alternative method that fixes the nozzle head and uses several pipe bends that flex under heating loads. The stand compensates for this growth using several high strength linear rails providing a rigid single degree of freedom system in the axial direction only (z-axis). The x and y directions are securely fastened to prevent unwanted oscillations induced by the large pressure differential between the nozzle and the chamber from disturbing the location of the jet's axis.

The placement of the nozzle's lip is crucial for preventing the shear layer from extending beyond the dimensions of the exhaust inlet. An angle of 15° w/r to the jet's axis is used to estimate this location. This is necessary to prevent unwanted flow re-circulations from occurring inside the chamber because of the anti-symmetric location of the chamber walls with respect to the jet's axis.

## G. Process Instrumentation and Control

The process for controlling the air supplied by the compressor / storage tanks to the experimental rig in the chamber is of immense importance especially for experimental studies at elevated temperatures. This is because the electric heater requires a bypass flow (experimen-

tal air supplied by the compressor) during all stages of its operation (including heat up and cool down) to prevent risk of destroying heater rods. The entire process is controlled using a Pro-Logix Control (PLC) arrangement with various sources of inputs listed as follows:

1. P1, tank pressure.
2. P2, static pressure in nozzle.
3. P3, total pressure in nozzle.
4. P4, plenum pressure, barometric.
5. P5, chamber pressure, barometric.
6. T1, nozzle temperature.
7. T2, chamber temperature.
8. FS, flow switch on/off, binary output.

The process for running cold experiments (no electrical heating) begins with the sensing of the tank pressure from P1. When a desired pressure is achieved in the 5 tanks (above 400psi or 2,760kPa), the control valve is throttled open in order to reach a pressure ratio between P2 / P5 corresponding to a desirable experimental condition. This relationship between P2 and P5 is based on a calibration performed before hand that determines the relationship between the total pressure at the center of the jet's exit measured by P3 (a total pressure probe is temporarily placed for this), and the static pressure in the pipe measured by P2. The relationship between P3 and P2 are also independent of ambient conditions and can be used reliably for remaining experiments.

With the exhaust fan operating, the make up air unit is activated for a given output temperature for the plenum bypass air. The variable frequency drive of the MUA fan is determined based on a ratio P4 / P5 close to unity. During this stage, much attention is given in order to maintain a pressure balance between the plenum (P4) and chamber (P5) as to prevent surging / overloading of the eductor fan, which may ultimately influence the natural entrainment and growth of the jet's shear layer. When the tank pressure drops below a certain level, the control valve is throttled shut and the compressor continues to recharge the tanks for the next experiment. The alternative process for running heated experiments is more crucial and involves bypass flow through the heater for reasons mentioned earlier. With the tanks fully charged, and the compressor still running, the control valve is opened and a bypass air is provided to the heater at a rate equal to the compressor's output. This prevents the tanks from deflating and provides adequate cooling needed to maintain safe operation of the electric heater during the heat up stage. Also the bypass air activates a flow switch, FS in the piping thus giving permission to the PLC to activate the heater. Output temperature is sensed by T1, whereas the chamber temperature is sensed by T2. Knowledge of the latter is crucial to ensure a safe environment for the delicate instruments. The sensing of T1, T2, P1, P2 and P5 is continuously monitored to achieve the desired operating conditions for the experiment. Also, the barometric sensor P4 is monitored to control the MUA fan speed and output temperature. The output temperature of the MUA unit is self-monitoring. For experiments exceeding the discharge rate of the compressor, (anything above  $M = 0.2$  for the 2 inch nozzle), the heater is shut down prematurely in order to ensure an ample supply of bypass air necessary to remove heat from the rods during cool down.

## H. Instrumentation

The appropriate hardware and software needed to capture the far field noise, the jet's turbulent shear layer, and the jet's fluctuating lip pressure, involve several independent devices. Two internal PCI A/D boards, each capable of sampling at 500kHz are able to sample an array of 6 x 1/4-inch microphones (166dB. dynamic range, 4Hz to 100kHz frequency response, +/- 2dB.) located along an arch separated by increments of 15°, starting with 15° from the jet axis. Utilizing anti-aliasing filters, we are able to resolve 83.3kHz from each microphone. Additional measurements will sample 1 x 1/8-inch microphone at 500kHz in order to capture a clear picture of the acoustic energy distribution of the jet's far field. The 15 pressure transducers (Kulite miniatures-0.093inch, 5psig) are sampled via a National Instruments PXI-system equipped with 2 x 4472-A/D boards, each channel capable of sampling at 100kHz. All of the instrument acquisition is triggered from the 200 mJ YAG laser to ensure simultaneous acquisition. The YAG laser illuminates 1-mm particles (olive oil for the cold jet) along several  $r, \theta$  planes downstream from the jet lip. The arrangement of the instrumentation is shown in figure 15 with respect to the jet. A recent discussion pertaining to the selection of instrumentation for accurate acoustical measurements in high speed jet facilities is presented by Ahuja<sup>24</sup>

## I. Jet Profile Measurements

Typical mean streamwise profiles at Mach 0.30, 0.60 and 0.85 at a jet stagnation temperature of 75° F are shown in figure 1 using a pitot tube, and similarity variables suggested by Mollo-Christensen *et al.*<sup>10</sup> The similarity variable  $\eta_s = 1 - (2r/D)/z$ , where  $z$  is the downstream distance from the nozzle exit plane and  $r$  is the distance from the center of the mixing layer, has collapsed the profiles for all Mach numbers and streamwise positions. Similar profiles are shown by Ponton *et al.*<sup>55</sup> for an axisymmetric 2 - inch nozzle at Mach 0.30, 0.60 and 0.85 at a "cold" jet stagnation temperature of 40° C using CTA tools.

Far field plume measurements are shown by Tinney *et al.*<sup>16</sup> using the  $5e^{-4}mmHg$ . accurate manometer mentioned earlier, and exhibit the jet plume's downstream development at  $20D$  to  $80D$ . These measurements employed a relatively coarse grid with the smallest radial spacing being of the order of  $\delta r/D = 0.5$ . The results confirmed symmetry of the jet's flow in the far field while a range of co-flow speeds were introduced with the MUA unit. A MUA fan speed of 85% and jet Mach number exit speeds of 0.60 and 0.85 correspond to a 3% and 2% co-flow, respectively.

Similar profile measurements using the PIV system are shown in figures 2 and 5 illustrating typical mean streamwise and secondary moment velocities, along with the profiles in similarity variables from Mollo-Christensen *et al.*<sup>10</sup> A total of 1,250 PIV snap shots are transformed into cylindrical coordinates (88x64 cartesian grid to  $96(r) \times 92(\theta)$  cylindrical grid) and are averaged in azimuth to create these half profiles. The mean streamwise profiles match that of the pitot tube and LDV system (regardless of the LDV's attenuation at this Mach number), and the turbulence intensities characterize the same growth patterns in  $r$  with an auto coherence peak at  $\frac{r}{R} = 1$ . Cross coherence measurements are discussed in later chapters pertaining to the modal decomposition.

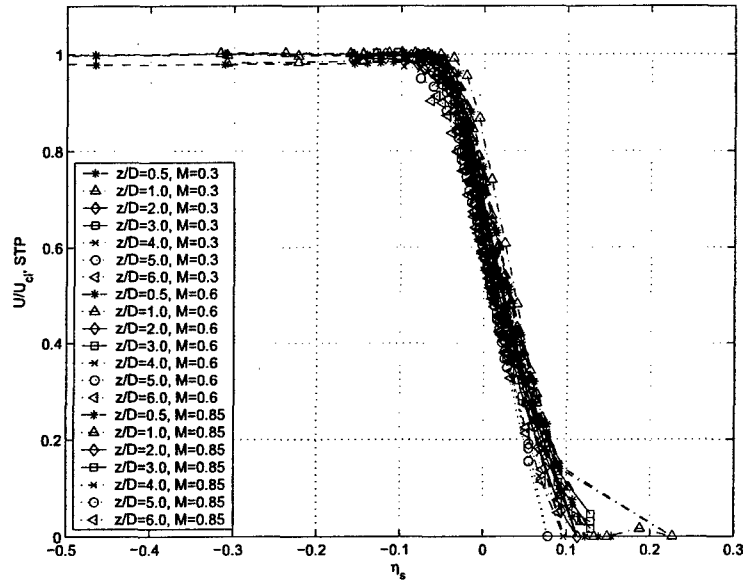


Figure 1. Streamwise velocity in similarity variables from pitot-static tube.

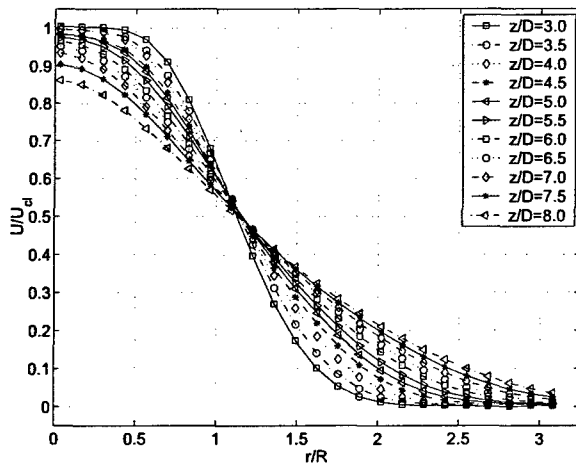


Figure 2. Mean streamwise velocity profile using PIV at Mach 0.85.

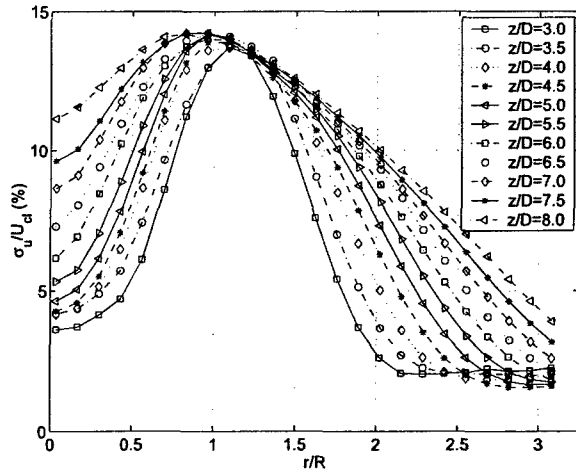


Figure 3. Streamwise turbulence intensity profile using PIV at Mach 0.85.

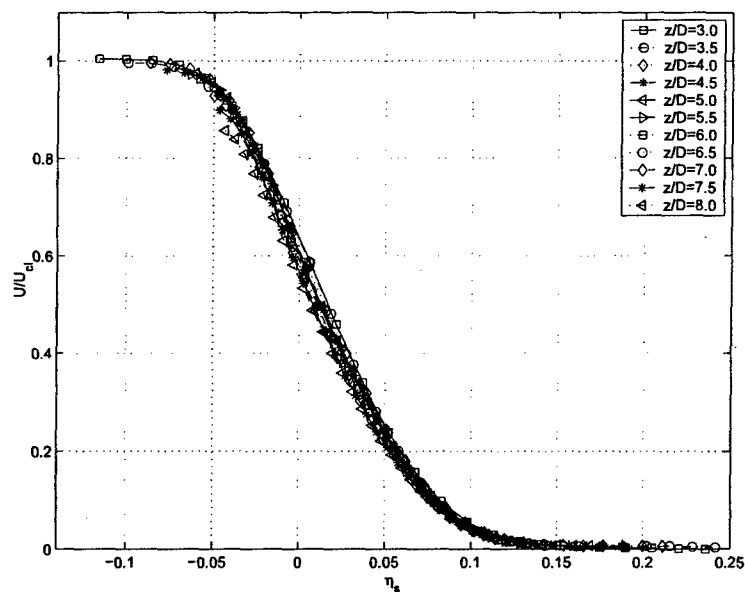


Figure 4. Streamwise mean velocity in similarity variables from PIV.

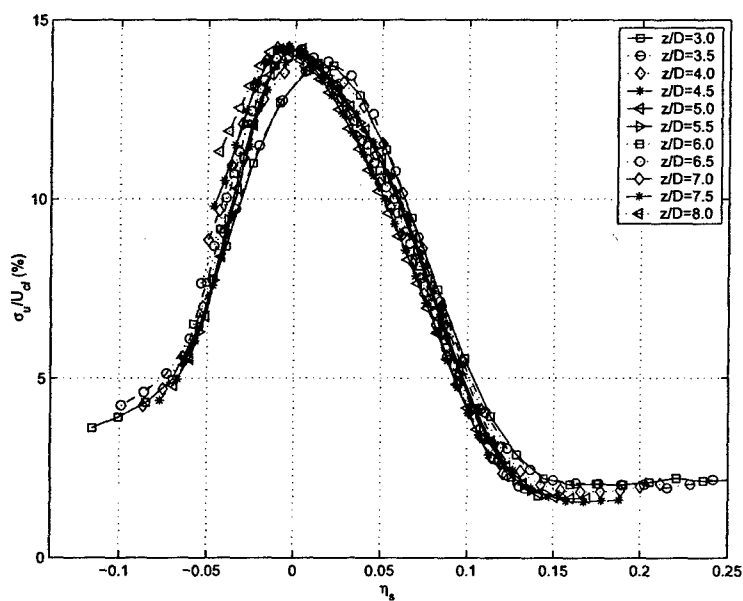


Figure 5. Streamwise r.m.s velocity in similarity variables from PIV.

## J. Far Field Acoustics

A survey of the far field acoustics utilized an arrangement of the *G.R.A.S.*  $\frac{1}{4}$  inch microphones. Their orientation in the chamber along a boom array at  $\frac{r}{D} = 75$  is shown in figure 6 with respect to the jet axis. Several laboratory conditions were investigated in order to identify any contaminating sources of noise. In particular, the MUA unit for a range of fan speeds, the eductor fan (either on or off), and the jet for a range of subsonic Mach numbers.

Time series data from the six microphones are acquired using the *UEI* data acquisition boards in conjunction with the *Khrone - Hite* band pass filters. The sampling rate for each channel is  $150kHz$  and is low pass filtered at  $75kHz$ . All spectral plots are created using 4,096 samples per block and are averaged over 100 total blocks. Based on these sampling conditions, the spectral resolution  $\delta f$  is  $36.6Hz$  with a total acquisition time of 2.7s. Before each experiment, the microphone's response function is checked with the piston-phone calibrator to ensure accurate and consistent measurements.

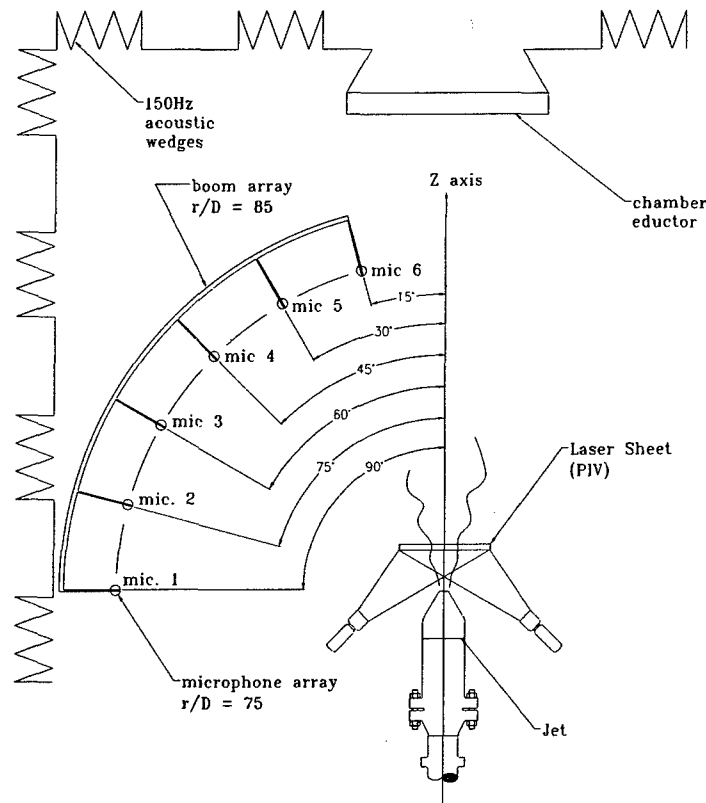


Figure 6. Layout of jet and instrumentation in the chamber.

Beginning with the facility's base sound pressure level (SPL), shown in figure 7, we can see that the noise floor is flat for all spectral frequencies measured, and is less than  $45dB$ . This also serves as an opportunity to view the microphone's thermal noise characteristics described earlier. With the eductor fan turned on, and for a range of MUA fan speeds (full range from 50% to 100% fan blade speed), the SPL remains the same. The exit co-flow

temperature ( $T_{cf}$ ) is  $75^{\circ}F$ .

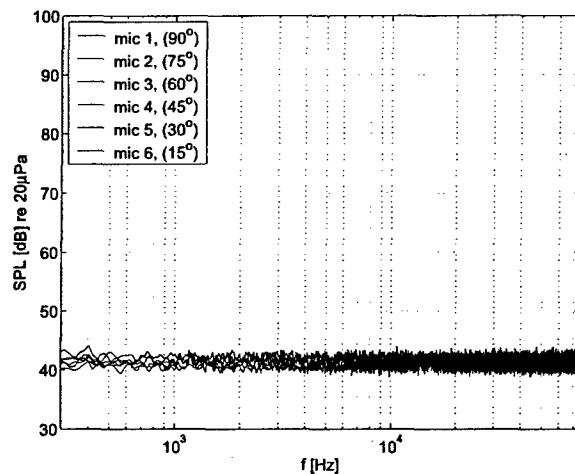


Figure 7. Facility base SPL spectrum.

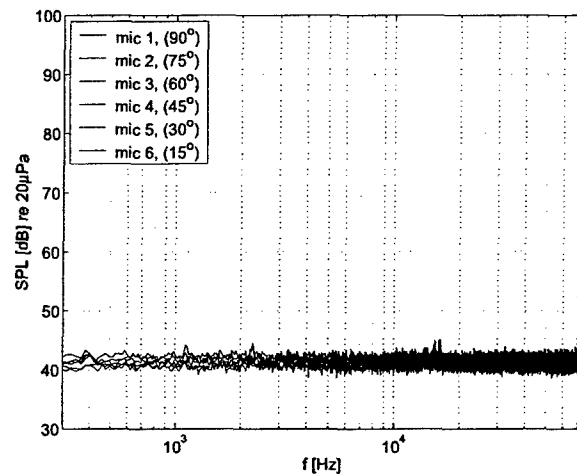


Figure 8. Eductor SPL spectrum.

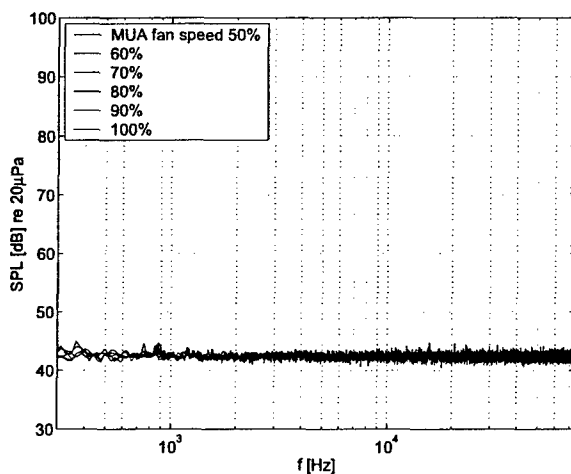


Figure 9. MUA unit SPL, mic 6, 50% to 100% fan blade speeds.

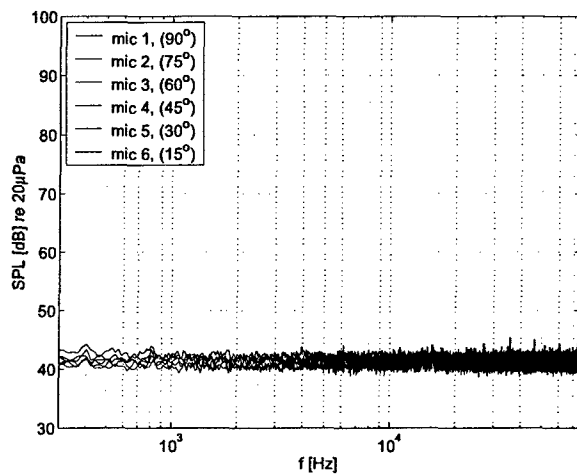


Figure 10. New base SPL conditions with MUA unit at 85%, eductor fan on,  $T_{cf} = 75^{\circ}$

In accordance with ISO 3745 standards, the facility is currently being tested using a hemispherical sound source for a range of frequencies using  $\frac{1}{3}$  octave scales:  $125Hz$ ,  $250Hz$ ,  $500Hz$ ,  $1kHz$ ,  $2kHz$  and  $4kHz$ . The inverse square decay law is currently being validated for this range of frequencies. Since the original investigations of Dosanjh *et al.*,<sup>34</sup> the interior chamber has had only minor changes. The recent rehabilitation effort was focused more on exterior items (MUA unit,  $460kW$  heater, control valve). Therefore, we do not anticipate any changes and will not wait for the facility's ISO validation to continue further with this study.

A range of jet exit speeds were investigated to gain some sense of the jet's acoustical characteristics and are shown in figure 11. The jet heater is not turned on and a small temperature gradient between the jet core and the co-flow exists.

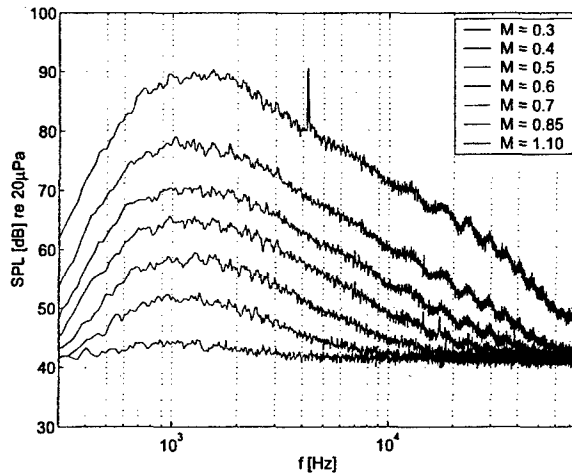


Figure 11. Jet SPL spectrum for a range of mach numbers recorded by microphone 5, (30°)

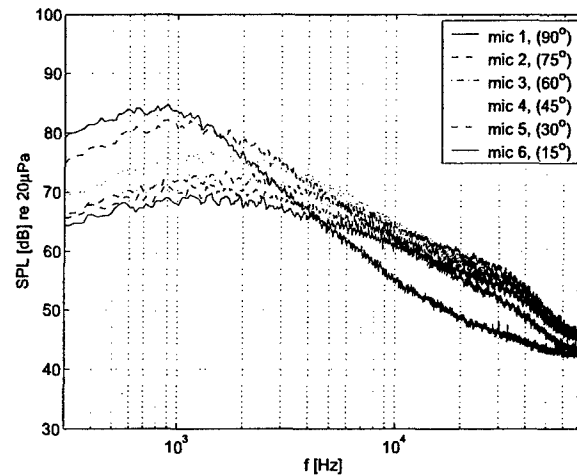


Figure 12. Corrected ripple in jet SPL spectrum at Mach 0.85,  $T_{cf} = 75^\circ F$ ,  $T_{jet} = 55^\circ F$ .

The ripple, shown most notably in figure 11 is a result of sound reflection from the microphone holder and has since been corrected. Figure 12 corresponds to far field noise measurements at Mach 0.85 jet exit speeds and illustrates the identification and removal of the contaminating reflection. Acoustic measurements were also performed at Mach 1.10 where shock structures are more evident than in high transonic jet flows. The far field acoustic spectrum incident to the axis of the jet clearly captures the original shock tone with its first harmonic. At a smaller angle along the jet's directive sound path (around 30° from the jet axis), only the first harmonic tone is captured. Tam<sup>60</sup> attributed this phenomena to Mach wave radiation, whereby the directivity of the sound field is warped by a combination of the large density gradients and the large scale structures in the shear layer.

The spectrum of acoustic energy illustrated here shifts energy from the high frequencies experienced by the observer in the far field at 90° to the jet axis, to lower frequency noise experienced by an observer at 15°. This shift in energy follows that of the classical phenomenon found in high speed jet noise whereby large wavelength structures produce the low frequency noise and the small wave length structures produce the higher frequency noise.

## VI. Velocity Field Decomposition

### A. Two-point Correlations

Since the two point correlations form the basis of the decomposition technique, it would be appropriate to illustrate their characteristics in the high speed subsonic jet for completeness. Hence, we will use this opportunity to display the two-point Reynolds stresses in cylindrical coordinates, from which the kernel is created, and the basis functions  $\phi_i^{(n)}(r, m, z_o)$  are solved. These correlations contain the necessary spatial relationships, in a mean square sense, between the turbulent motions of the flow, and is what makes the POD and the joint decomposition techniques powerful tools in turbulence. Therefore, the cross correlation

relation between these points can inscribe essential characteristics about the flow that is distinguishable from other large eddy identification techniques.

The stress terms are generated from 1,250 PIV snap shots of the velocity field's  $r, \theta$  cross plane, taken along the sound source regions of the flow, with streamwise spacing  $\Delta z = 0.25D$ . The timing between snap shots is 0.25s. Since the dominant time scales in the flow are of order  $3e^{-3}s$ , the sampling rate of the PIV system is clearly shown to preserve statistical independence. This is important since we are dealing with a limited number of samples.

Each PIV stereo vector field is originally in a cartesian grid formed from 69 ( $x$ ) by 105 ( $y$ ) points that does not change with changing position (in  $z$ ). After re-centering and sub-sampling in  $y$ , the template grid density (that we will be working with for the remainder of this investigation) is 66 ( $x$ ) by 51 ( $y$ ) where  $\Delta x$  and  $\Delta y$  are 2.56mm ( $5.0e^{-2}D$ ) and 3.37mm ( $6.6e^{-2}D$ ) respectively. The transformation from cartesian to cylindrical coordinates yields a different grid density of 27 ( $r$ ) by 90 ( $\theta$ ), with  $4^\circ$  of separation in azimuth and  $\Delta r = 0.5(\Delta x + \Delta y)$ . This transformation is based on the template grid density and was carefully selected to preserve the original scales of the flow. Should one use a courser grid (relative to the original PIV grid), the smaller scale events that were otherwise captured via PIV, are removed and forever lost; whereas, a denser grid assumes relationships between scales smaller than the original grid's resolution, that may otherwise be incorrect.

The azimuthal correlations are averaged in azimuth to ensure azimuthal symmetry using a given azimuthal separation,  $\Delta\theta$  taken as the difference between  $\theta_o$  and  $\theta'$ . This is sometimes necessary to account for any discrepancies that may have incurred using experimental techniques with limited sample sets.

*The kernel created for the 2-d scalar POD is not shown, as it is not as insightful as the kernel generated for the "joint" decomposition using the jet's mean azimuthal characteristics.*

Two different plotting styles are used to illustrate the magnitude of the kernel's spatial decay along the  $r, \theta$  plane in figures 13 through 24. On the left and right hand sides are surface mesh plots (to characterize the kernel's mean azimuthal invariance) and their corresponding normalized magnitude (normalized by the kernel's maximum value). The maximum value for a given streamwise location for  $r = r'$  is commonly found along the center of the mixing layer at  $\frac{r}{R} = 1$ . The antisymmetry in  $r$  is also shown and exhibits the differences in the shear layer's growth rate.

The two-point Reynolds shear stress terms,  $uv$  are shown similarly in figures 19 to 24 and exhibit the same behaviors as the normal stress terms regarding jet spreading and the locations of the peak amplitudes.

## B. Low-Dimensional Behavior

### 1. 2-d Scalar POD

We will present and discuss the application of the 2-d scalar POD ( $u$ -component only) in brief. The results are shown in figure 25 for the discrete applications at  $\frac{z}{D} = 3, 4, 5, 6, 7$  and 8. In doing so, the decomposition of the axisymmetric mixing layer will be treated as a fully inhomogeneous flow, (assuming no mean azimuthal invariance!) and the POD technique will be applied over the entire domain of interest.

The eigenspectra are shown to decay rapidly with increasing mode number for all stream-wise positions studied. We find that with 100 POD modes, which account for less than 3%

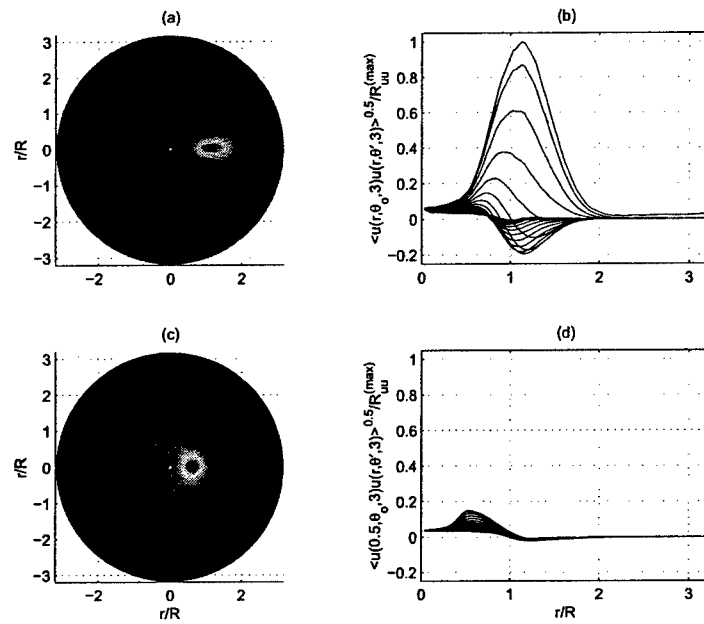


Figure 13. The  $R_{uu}$  correlation function, (a.) surface mesh of  $R_{uu}(r, r' = r, \theta_o + \Delta\theta, 3)$ , (b.) of (a.) normalized by max. value in  $R_{uu}$ , (c.) surface mesh of  $R_{uu}(r = 0.5, r', \theta_o + \Delta\theta, 3)$ , (d.) of (c.) normalized by max. value in  $R_{uu}$ .

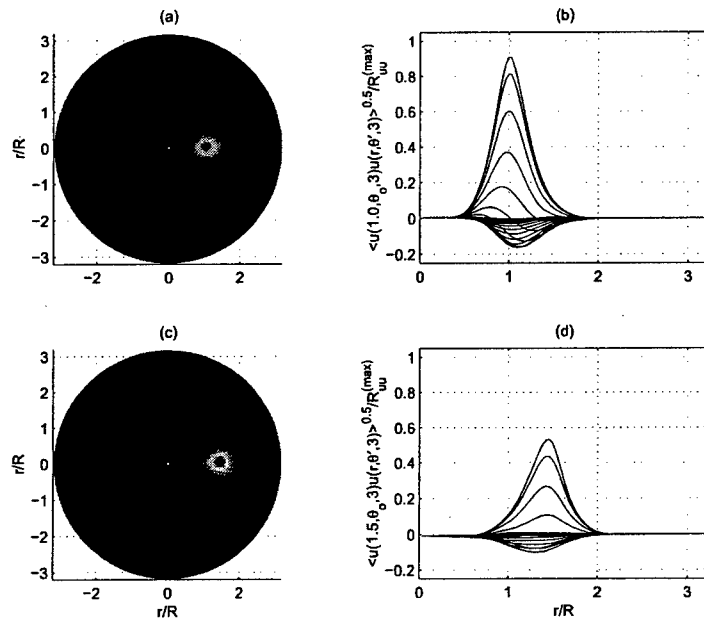


Figure 14. The  $R_{uu}$  correlation function, (a.) surface mesh of  $R_{uu}(r = 1.0, r', \theta_o + \Delta\theta, 3)$ , (b.) of (a.) normalized by max. value in  $R_{uu}$ , (c.) surface mesh of  $R_{uu}(r = 1.5, r', \theta_o + \Delta\theta, 3)$ , (d.) of (c.) normalized by max. value in  $R_{uu}$ .

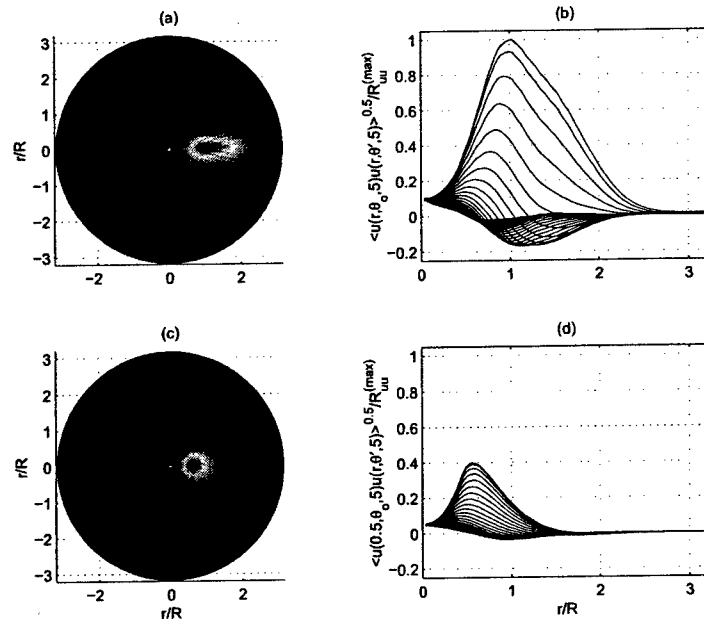


Figure 15. The  $R_{uu}$  correlation function, (a.) surface mesh of  $R_{uu}(r, r' = r, \theta_o + \Delta\theta, 5)$ , (b.) of (a.) normalized by max. value in  $R_{uu}$ , (c.) surface mesh of  $R_{uu}(r = 0.5, r', \theta_o + \Delta\theta, 5)$ , (d.) of (c.) normalized by max. value in  $R_{uu}$ .

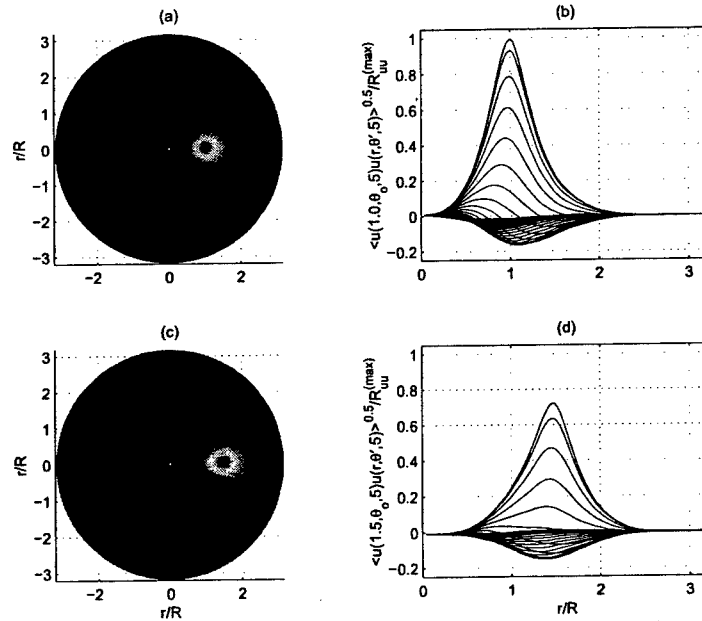


Figure 16. The  $R_{uu}$  correlation function, (a.) surface mesh of  $R_{uu}(r = 1.0, r', \theta_o + \Delta\theta, 5)$ , (b.) of (a.) normalized by max. value in  $R_{uu}$ , (c.) surface mesh of  $R_{uu}(r = 1.5, r', \theta_o + \Delta\theta, 5)$ , (d.) of (c.) normalized by max. value in  $R_{uu}$ .

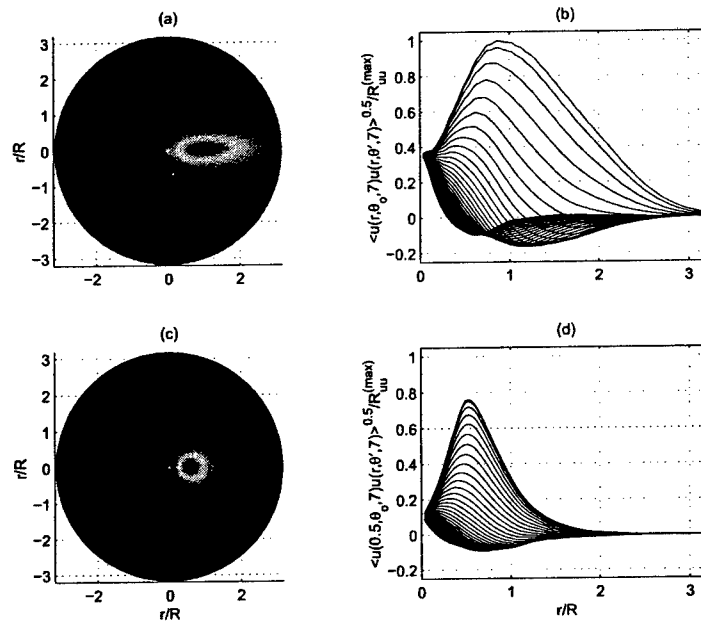


Figure 17. The  $R_{uu}$  correlation function, (a.) surface mesh of  $R_{uu}(r, r' = r, \theta_o + \Delta\theta, 7)$ , (b.) of (a.) normalized by max. value in  $R_{uu}$ , (c.) surface mesh of  $R_{uu}(r = 0.5, r', \theta_o + \Delta\theta, 7)$ , (d.) of (c.) normalized by max. value in  $R_{uu}$ .

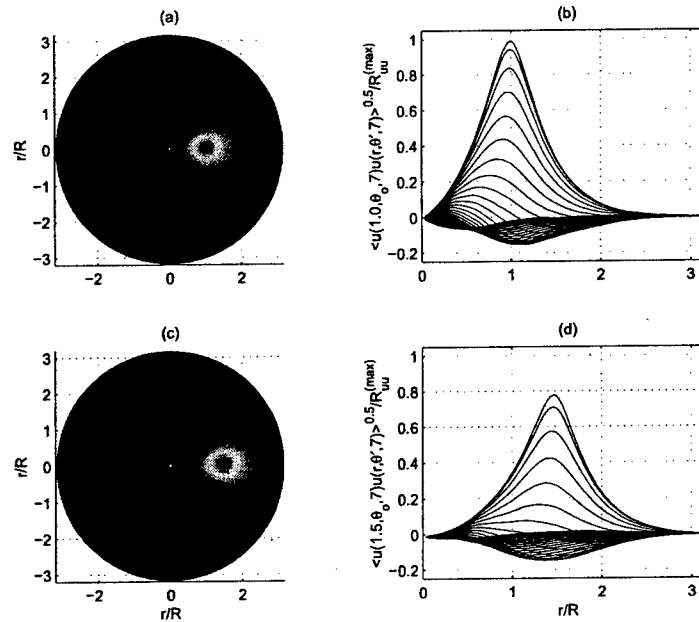


Figure 18. The  $R_{uu}$  correlation function, (a.) surface mesh of  $R_{uu}(r = 1.0, r', \theta_o + \Delta\theta, 7)$ , (b.) of (a.) normalized by max. value in  $R_{uu}$ , (c.) surface mesh of  $R_{uu}(r = 1.5, r', \theta_o + \Delta\theta, 7)$ , (d.) of (c.) normalized by max. value in  $R_{uu}$ .

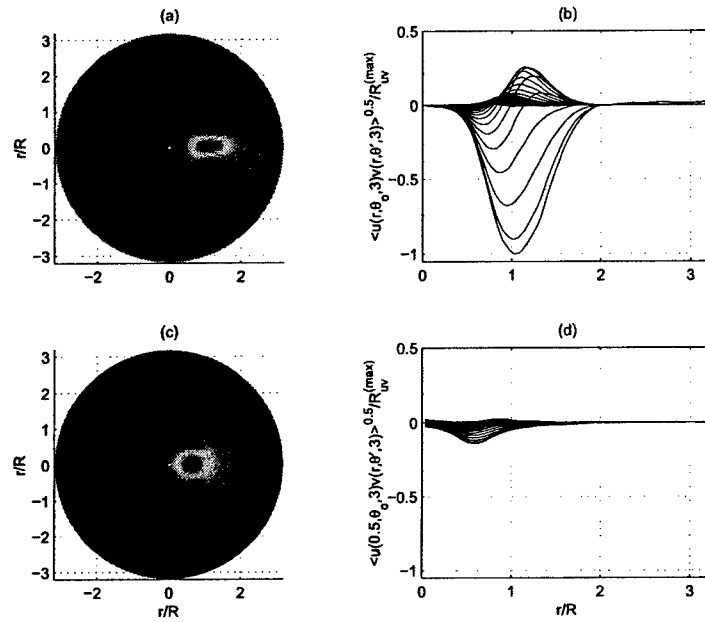


Figure 19. The  $R_{uv}$  correlation function, (a.) surface mesh of  $R_{uv}(r, r' = r, \theta_o + \Delta\theta, 3)$ , (b.) of (a.) normalized by max. value in  $R_{uv}$ , (c.) surface mesh of  $R_{uv}(r = 0.5, r', \theta_o + \Delta\theta, 3)$ , (d.) of (c.) normalized by max. value in  $R_{uv}$ .

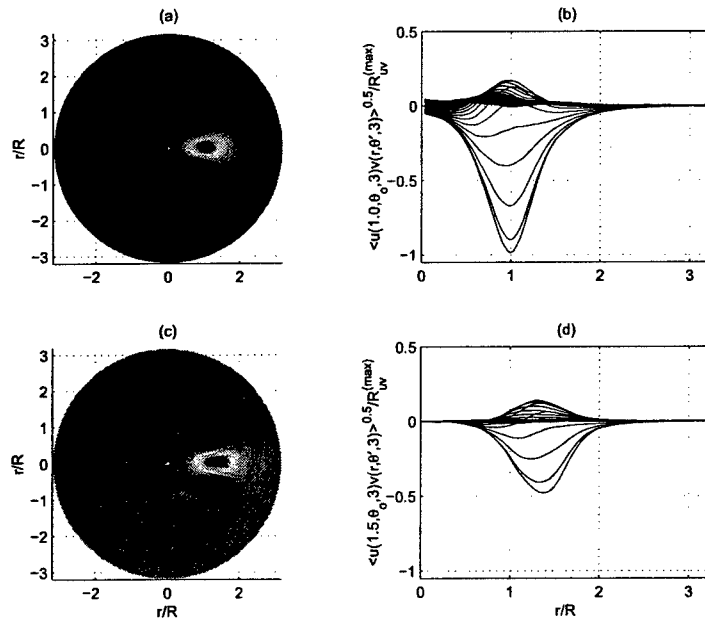


Figure 20. The  $R_{uv}$  correlation function, (a.) surface mesh of  $R_{uv}(r = 1.0, r', \theta_o + \Delta\theta, 3)$ , (b.) of (a.) normalized by max. value in  $R_{uv}$ , (c.) surface mesh of  $R_{uv}(r = 1.5, r', \theta_o + \Delta\theta, 3)$ , (d.) of (c.) normalized by max. value in  $R_{uv}$ .

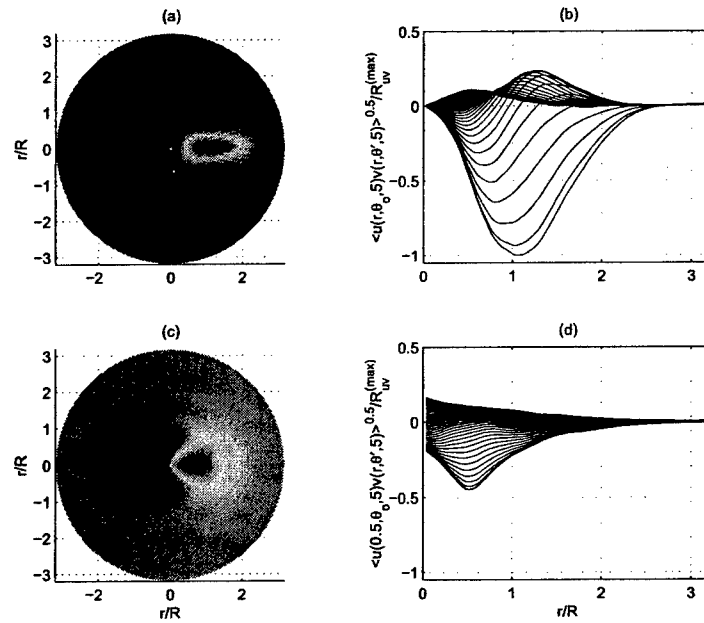


Figure 21. The  $R_{uv}$  correlation function, (a.) surface mesh of  $R_{uv}(r, r' = r, \theta_o + \Delta\theta, 5)$ , (b.) of (a.) normalized by max. value in  $R_{uv}$ , (c.) surface mesh of  $R_{uv}(r = 0.5, r', \theta_o + \Delta\theta, 5)$ , (d.) of (c.) normalized by max. value in  $R_{uv}$ .

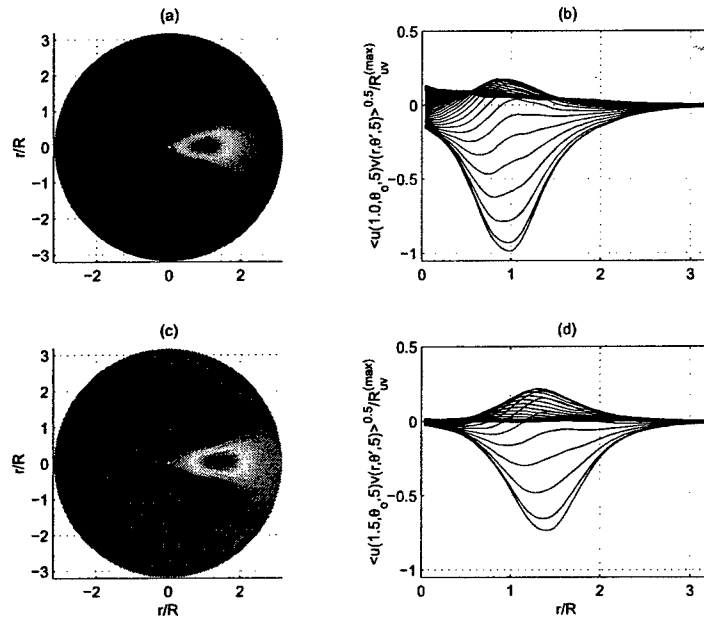


Figure 22. The  $R_{uv}$  correlation function, (a.) surface mesh of  $R_{uv}(r = 1.0, r', \theta_o + \Delta\theta, 5)$ , (b.) of (a.) normalized by max. value in  $R_{uv}$ , (c.) surface mesh of  $R_{uv}(r = 1.5, r', \theta_o + \Delta\theta, 5)$ , (d.) of (c.) normalized by max. value in  $R_{uv}$ .

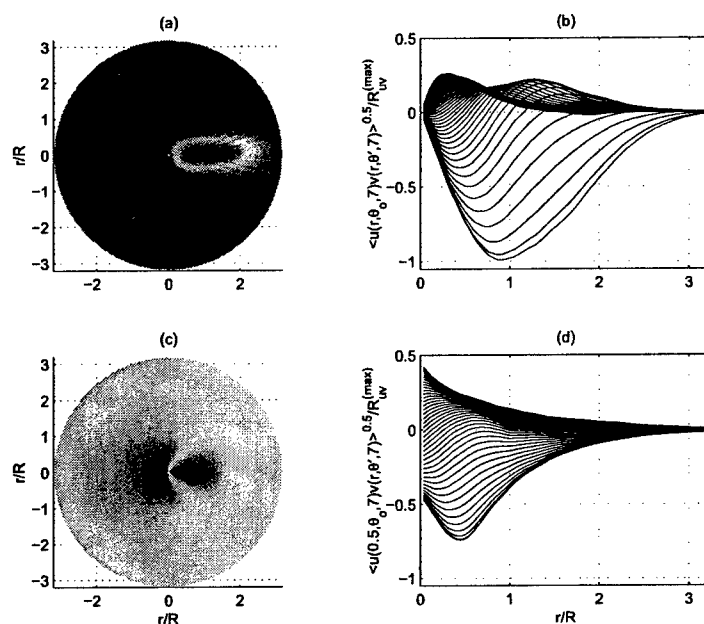


Figure 23. The  $R_{uv}$  correlation function, (a.) surface mesh of  $R_{uv}(r, r' = r, \theta_o + \Delta\theta, 7)$ , (b.) of (a.) normalized by max. value in  $R_{uv}$ , (c.) surface mesh of  $R_{uv}(r = 0.5, r', \theta_o + \Delta\theta, 7)$ , (d.) of (c.) normalized by max. value in  $R_{uv}$ .

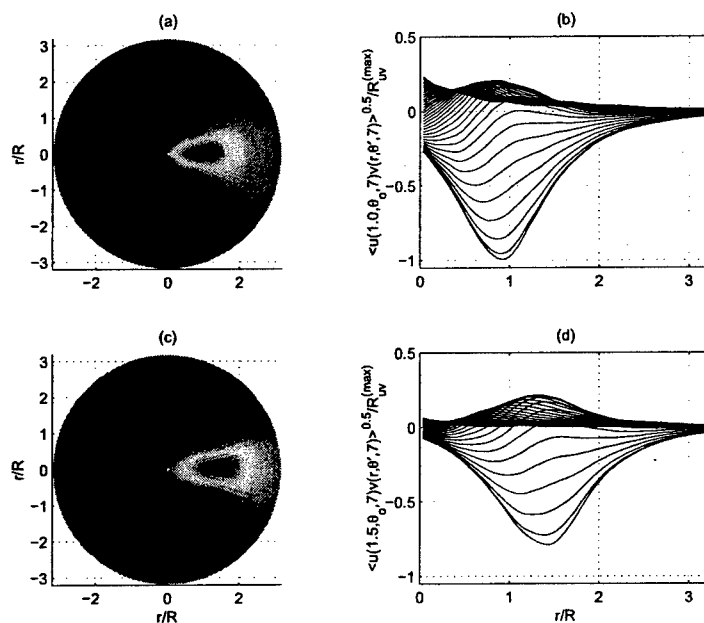


Figure 24. The  $R_{uv}$  correlation function, (a.) surface mesh of  $R_{uv}(r = 1.0, r', \theta_o + \Delta\theta, 7)$ , (b.) of (a.) normalized by max. value in  $R_{uv}$ , (c.) surface mesh of  $R_{uv}(r = 1.5, r', \theta_o + \Delta\theta, 7)$ , (d.) of (c.) normalized by max. value in  $R_{uv}$ .

of the 3,366 total modes, roughly 70% of the turbulent kinetic energy, can be restored. It is impressive to see such a rapid convergence of the jet's large scale motions using this form of the decomposition technique. Convergence of the solution is found to have little change over the streamwise positions studied. The upper dashed trend is the incrementally-combined energy and increases in the abscissa in the direction of increasing streamwise position.

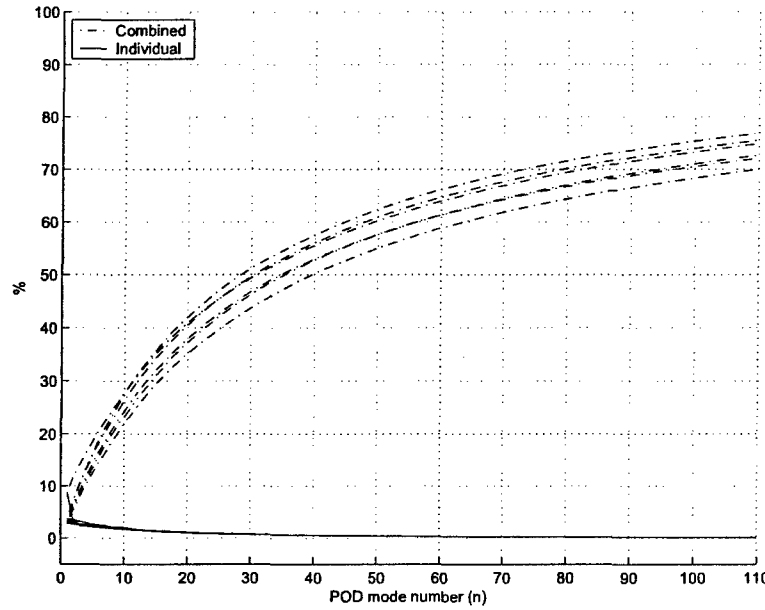


Figure 25. Eigenspectra from  $\frac{z}{D} = 3.00$  to 8.00 using the 2-d scalar POD. A larger amplitude in the abscissa is in the direction of increasing streamwise position.

## 2. Joint Decomposition Methods

To best illustrate the relative energy of the basis set, the eigenvalue solutions are normalized by the total energy at a given streamwise position in the flow. This is determined from equation 38 and applied to equation 39. The total number of modes in the *joint* scalar problem consists of  $n = 27$  POD and  $m = 45$  azimuthal modes (because of symmetry, the cosine transform is performed over  $M/2=m$  modes). Simple algebra tells us that a total of 1,215 total modes are created using the scalar form of the *joint* technique, 2,430 in the two-component vector form, and 3,645 in the three-component vector form.

$$\zeta(z) = \sum_n \sum_m \lambda^{(n)}(m, z) \quad (37)$$

$$\xi(n, z) = \frac{\sum_m \lambda^{(n)}(m, z)}{\zeta(z)} \quad (38)$$

or,

$$\Lambda^{(n)}(m, z) = \frac{\lambda^{(n)}(m, z)}{\zeta(z)} \times 100 \quad (39)$$

The normalized scalar eigenvalues presented in figures 26 to 28 are clearly shown to characterize the low dimensional azimuth behavior of the turbulent events in this flow. The azimuthal eigenspectra were not found to have any peaks beyond the mode numbers shown here. Therefore only the lower azimuthal modes are of interest to the investigation. It is important to point out that with the scalar form of this *joint* technique, the fifth, sixth and seventh azimuthal modes are found to contain most of the energy at the closest streamwise position studied (3D). However at farther positions (8D), the third azimuthal mode ( $m = 2$ ) has most of the mean square energy.

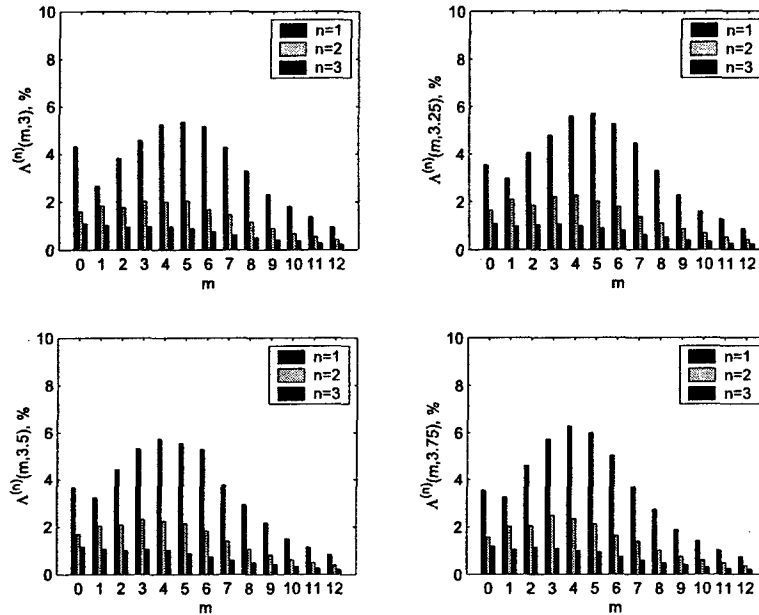


Figure 26. Eigenspectra from  $\frac{z}{D} = 3.00$  to  $3.75$  of  $n = 1 : 3$  and  $m = 0 : 12$  using scalar *joint* decomposition, (u component).

The solutions to the vector (two-component) *joint* decomposition shown in figure 29 are found to be similar to the findings of Ukeiley *et al.*<sup>18</sup> who studied the Mach 0.30 and 0.60 axisymmetric jet using the *joint* technique with streamwise ( $\rho u$ ) and radial ( $\rho v$ ) components of mass flux. It is appropriate to emphasize here that the additional component of velocity (for instance, the radial component shown here) merely adds more energy to all eigenmodes, as opposed to shifting energy to lower azimuthal modes. As a reminder, the *joint* application by Ukeiley *et al.*<sup>18</sup> used a slightly sparser grid density of  $\Delta\theta = 10^\circ$  with two radial rakes of cross wire probes. This is impressive if one appreciates that the results are obtained using two different facilities, under slightly different conditions, using a completely different arrangement of instrumentation. The *joint* decomposition using the full turbulent kinetic energy, is shown in figure 30.

### C. Low-Dimensional Reconstruction Using the Most Energetic Modes

Using the basis functions from the decomposition, a low-dimensional reconstruction of select PIV images is performed. Recall that the time difference between images exceeds several

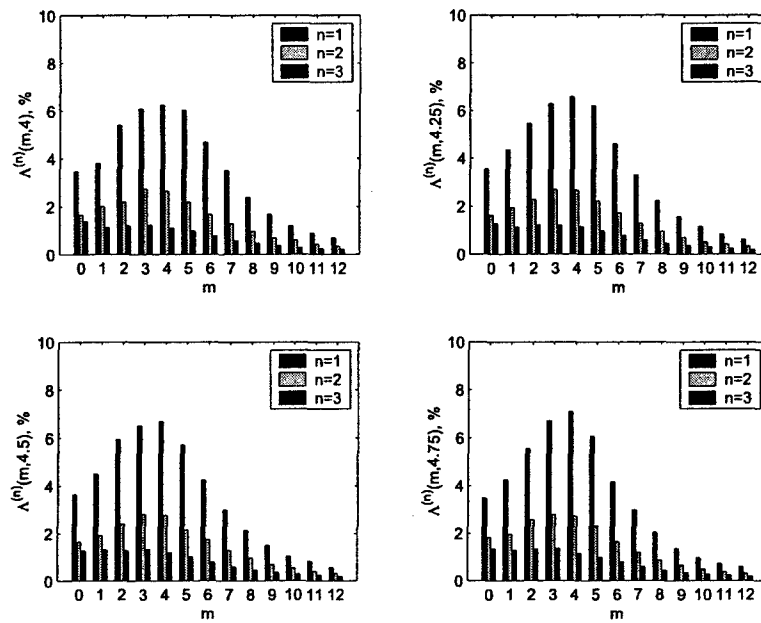


Figure 27. Eigenspectra from  $\frac{z}{D} = 4.00$  to 4.75 of  $n = 1 : 3$  and  $m = 0 : 12$  using scalar *joint* decomposition, (u component).

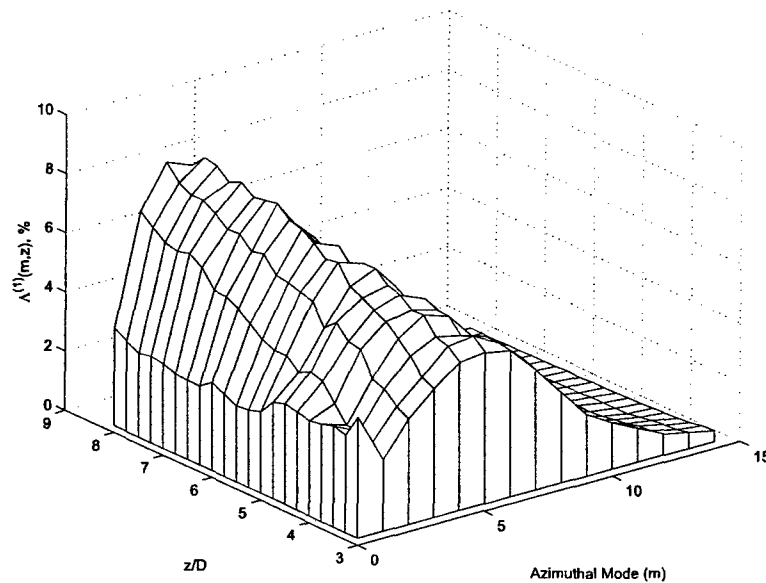


Figure 28. Eigenspectra distribution from  $\frac{z}{D} \approx 3.00$  to 8.00 of  $n = 1 : 3$  and  $m = 0 : 14$  using scalar *joint* decomposition, (u component).

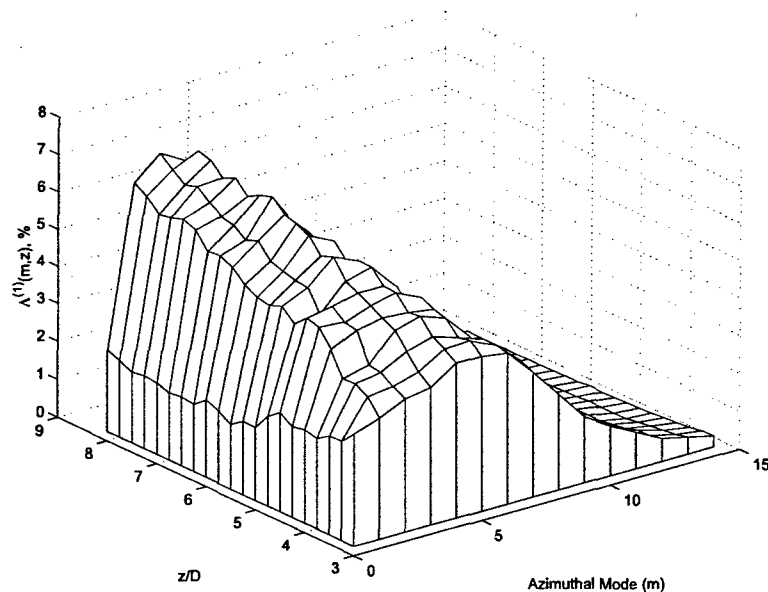


Figure 29. Eigenspectra distribution from  $\frac{z}{D} = 3.00$  to  $8.00$  of  $n = 1 : 3$  and  $m = 0 : 14$  using joint decomposition, (u&v components).

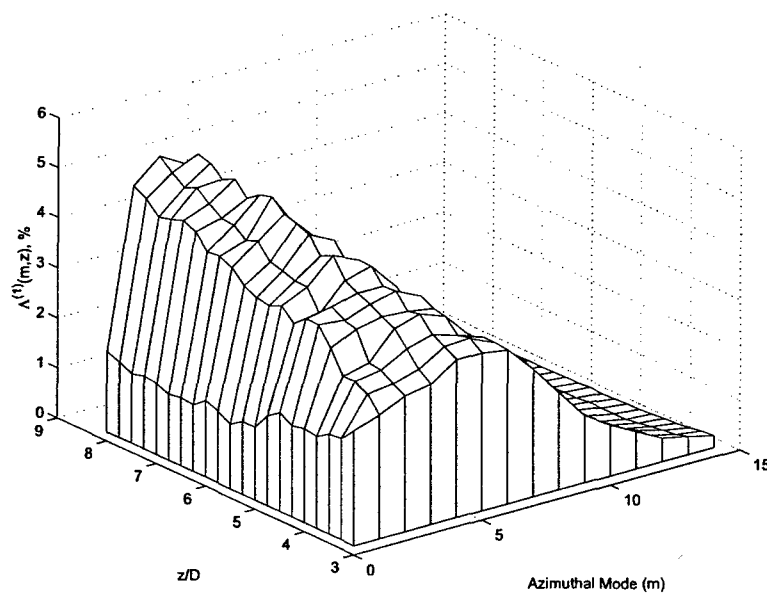


Figure 30. Eigenspectra distribution from  $\frac{z}{D} = 8.00$  to  $8.00$  of  $n = 1 : 3$  and  $m = 0 : 14$  using joint decomposition, (u,v&w components).

time scales of the flow, as is the motivation for employing the *MCT* techniques. Using the 2-d scalar POD, we are still capable of gaining some insight into the original characteristics of the turbulent events from this flow.

### 1. 2-d Scalar POD Reconstruction

In figure 31, original PIV cross-plane snap shots ( $r, \theta$ ) of the fluctuating velocity field ( $u$ -component) at Mach 0.85 and  $\frac{z}{D} = 3$  are shown at four discrete time steps. Next to this (figure 32), a low-dimensional reconstructions of these snap shots are shown using the scalar 2-d POD technique. A striking resemblance between the two figures illustrates the capabilities of the low-dimensional technique to capture the key features of the flow. The events are shown to possess the azimuthal behaviors found in flows from axisymmetric geometries. At this streamwise position, the relatively small turbulence levels in the core regions of the jet are visible. Further downstream at  $\frac{z}{D} = 5$  (figures 33 & 34) and  $\frac{z}{D} = 8$  (figures 35 & 36), similar behaviors are seen. Here the shear layer is shown to have grown noticeably, thus engulfing the potential core. The instantaneous turbulent events now cover a much broader region of the flow.

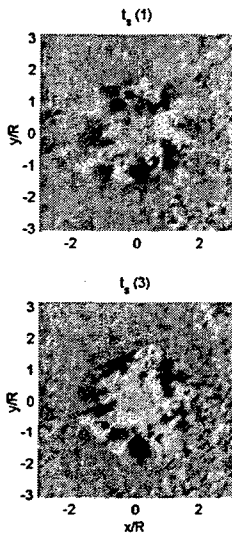


Figure 31. Original PIV cross-plane snap shot at four statistically independent time steps at  $\frac{z}{D} = 3$  and Mach 0.85.

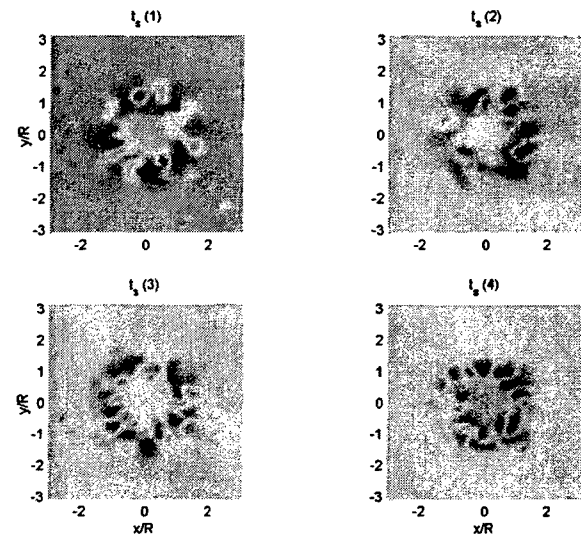


Figure 32. Low-dimensional reconstruction of figure 31 using 2-d scalar POD at  $\frac{z}{D} = 3$  with 100 POD modes (3% energy).

## VII. Modified Complementary Techniques using a Cross Spectral Tensor

The modified Complementary Techniques used in this investigation differs slightly from the original form proposed earlier. This is because coherence between the near field lip pressure and the *joint* expansion coefficients (velocity field) requires a crucial phasing coefficient  $\tau$  based on the transport speed of the turbulent events. Therefore, by incorporating a full

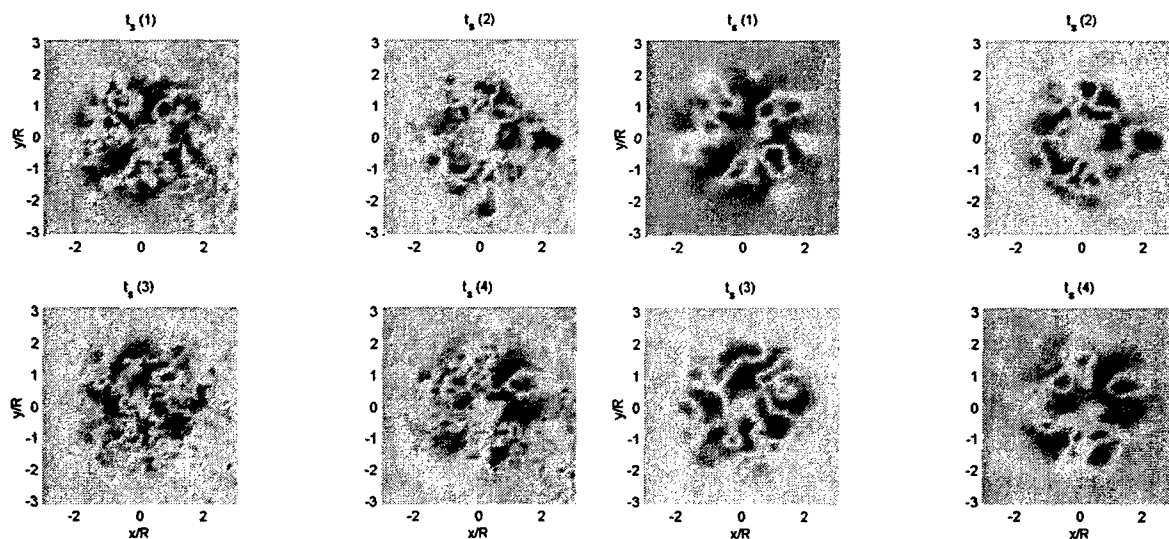


Figure 33. Original PIV cross-plane snap shot at four statistically independent time steps at  $\frac{z}{D} = 5$  and Mach 0.85.

Figure 34. Low-dimensional reconstruction of figure 33 using 2-d scalar POD at  $\frac{z}{D} = 5$  with 100 POD modes (3% energy).

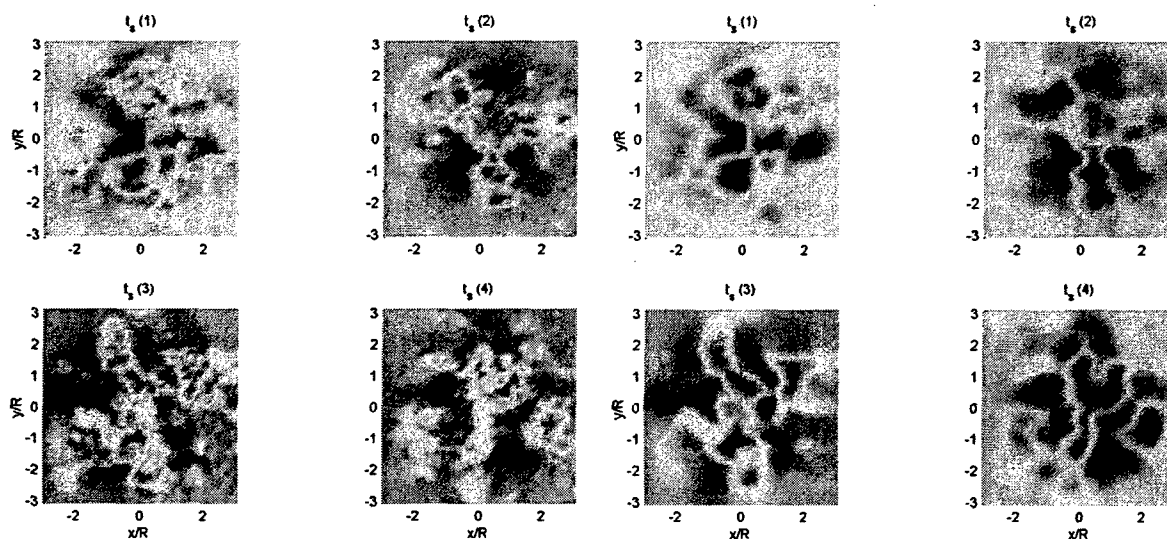


Figure 35. Original PIV cross-plane snap shot at four statistically independent time steps at  $\frac{z}{D} = 8$  and Mach 0.85.

Figure 36. Low-dimensional reconstruction of figure 35 using 2-d scalar POD at  $\frac{z}{D} = 8$  with 100 POD modes (3% energy).

measure of the cross spectral relationship between the *joint* expansion coefficients and the near field pressure, the necessary spatial and temporal phase characteristics of the final event estimate are greatly improved. This is shown as follows.

- The random expansion coefficients are calculated from the basis functions at each statistically independent time step, ( $t_s$ ) using multi-component forms of the *joint* decomposition technique. The kernel is generated using select components ( $c$ ) of the velocity field via the PIV snap shots.

$$\hat{a}_n(m, z_o, t_s) = \int_D u_c(r, m, z_o, t_s) \phi_c^{(n)}(r, m, z_o) dr \quad (40)$$

- From the simultaneous sampling of the hydrodynamic near field pressure (an azimuthal array of  $j = 15$  transducers near the jet's lip) with the *joint* expansion coefficients calculated from the PIV measurements, a cross correlation matrix is formed (over all  $t_s$  instances for all  $n$  and  $m$ ) and the cross spectral densities between these two scalar terms are computed.

$$\hat{S}_j(n, m, z_o, f) = \int \overline{p_j(t_s - \tau) \hat{a}_n(m, z_o, t_s)} e^{-i(2\pi f \tau)} d\tau \quad (41)$$

- Using the enormous time series data of the near field pressure, the cross spectral densities between all  $j$  and  $k$  transducers are determined, and the symmetric cross spectral correlation matrix is formed.

$$\hat{S}_{j,k}(f) = \overline{\hat{p}_j^*(f) \hat{p}_k(f)} \quad (42)$$

- Following the form of the *LSE* technique, such that  $[A][B] = [C]$ , the linear estimation coefficients are determined, where  $[B] = \hat{b}_j(n, m, z_o, f)$  and are complex.

$$\hat{b}_j(n, m, z_o, f) = \frac{[C]}{[A]} = \frac{\hat{S}_j(n, m, z_o, f)}{\hat{S}_{j,k}(f)} \quad (43)$$

- Expanding the estimation coefficients with the spectral form of the pressure data (these transducers are sampled at bandwidths capable of resolving the spectral characteristics of the sound source events), an estimate of the *joint* expansion coefficients are realized at continuous time intervals.

$$\hat{a}_n(m, z_o, t) = \frac{1}{2\pi} \int \left\{ \sum_j \hat{b}_j(n, m, z_o, f) \hat{p}_j(f) \right\} e^{i(2\pi f t)} df \quad (44)$$

- In the final step of the procedure, select modes ( $n$ ) are projected onto the *joint* expansion coefficients and the transformation from Fourier-azimuthal mode to azimuth provides a dynamical reconstruction of the more energetic events of the flow in the sound source regions.

$$\tilde{u}_c(r, m, z_o, t) = \sum_n \hat{a}_n(m, z_o, t) \phi_c^{(n)}(r, m, z_o) \quad (45)$$

$$\tilde{u}_c(r, \theta, z_o, t) = \frac{1}{2\pi} \int \tilde{u}_c(r, m, z_o, t) e^{i(2\pi m \theta)} dm \quad (46)$$

## A. Correlations

The focus of this section is to quantify the correlation between the *joint* expansion coefficients and the near field pressure, expressed in equation 41.

The magnitude of the cross correlation  $\hat{\rho}_{\Psi}(n, m, \tau, z, j)$  used to create the cross spectral density function in equation 41 is shown using the scalar form of the *joint* decomposition technique. This is normalized by the product between  $\sigma_p(\tau, j)$  and  $\sigma_a(n, m, z)$ , where the modulus of the expansion coefficient  $\sqrt{\Re \hat{a}(n, m, z)^2 + \Im \hat{a}(n, m, z)^2}$  and of the cross correlation function  $\sqrt{\Re \rho_p(\tau, j)^2 + \Im \rho_p(\tau, j)^2}$  are used. Results are shown averaged over all fifteen transducers and clearly articulates a decent correlation of 40% with the zeroeth azimuthal mode in figure 37 and 20% with the second azimuthal mode in figure 38. The first POD mode ( $n = 1$ ) is used in both instances. The convection speeds of these events, based on the space-time locations of the first peaks, is  $0.77U_d$  and  $0.67U_d$  for  $m = 0$  and  $m = 2$  modes, respectively. The convection speed for the  $m = 1$  mode (not shown) is  $0.73U_d$ . The trend suggests that the higher Fourier-azimuthal modes (small scale events) convect at slower speeds, as oppose to the lower modes (large scale events) that move much more rapidly (influenced by the speed of the potential core because they span over a larger radial distance). Glauser *et al.*<sup>4</sup> and Taylor *et al.*<sup>14</sup> were able to perform the decomposition using a cross-spectral tensor because of the CTA instruments employed in their investigation. From this they were able to illustrate that at Mach 0.6, the peak frequency of the  $m = 0$  mode was  $1.6kHz$  with a peak in the  $m = 8$  mode around  $200Hz$  and is similar to the trends observed with the space-time correlation function in the current investigation. These are complementary findings that are difficult to interpret under the classical theory of aerodynamically generated sound.

Oddly enough, an average of these trends over the first ten Fourier-azimuthal modes yields a higher transport speed around  $0.8U_d$ . The averaging normalizes each individual trend before-hand by the maximum of that trend. This is done to evenly weight the averaging so that no single modal trend could bias the average. The resultant convection speed warrants additional investigation.

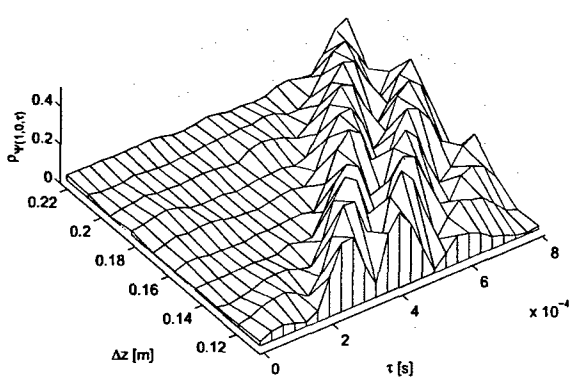


Figure 37. Space time correlation function for the  $m = 0$ , and  $n = 1$ , Mach 0.85, with near field pressure array using scalar *joint* decomposition.

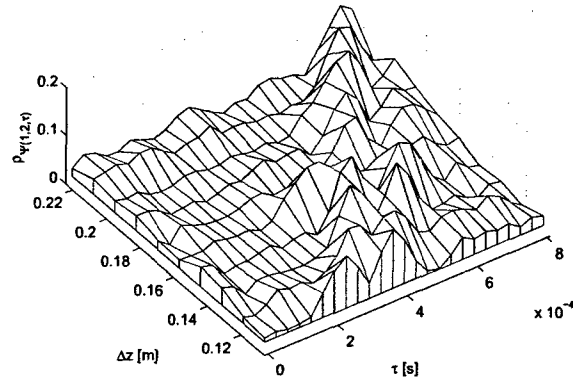


Figure 38. Space time correlation function for the  $m = 2$ , and  $n = 1$ , Mach 0.85, with near field pressure array using scalar *joint* decomposition.

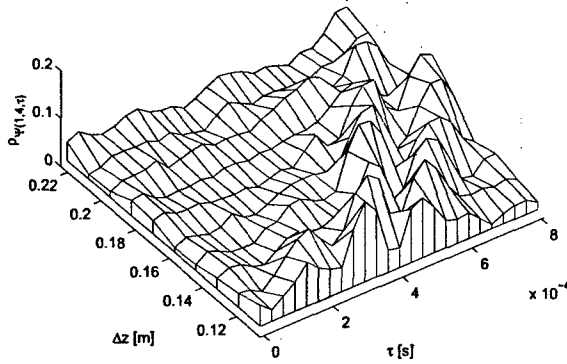


Figure 39. Space time correlation function for the  $m = 4$ , and  $n = 1$ , Mach 0.85, with near field pressure array using scalar *joint* decomposition.

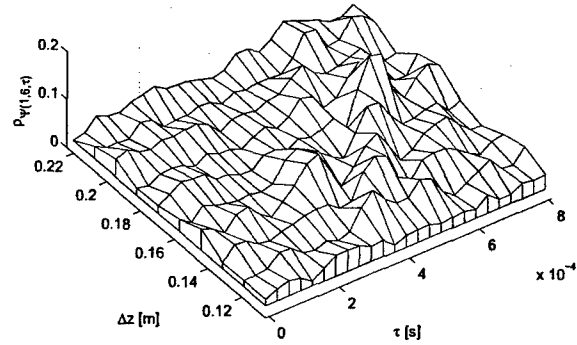


Figure 40. Space time correlation function for the  $m = 6$ , and  $n = 1$ , Mach 0.85, with near field pressure array using scalar *joint* decomposition.

## B. Cross-Spectral Densities

We will take this opportunity to preview the cross spectral densities,  $\hat{S}_j(n, m, z_o, f)$  and  $\hat{S}_{j,k}(f)$ , from equation 41 and 42, respectively. Since the raw spectral densities are calculated from a limited number of samples (1,250 PIV images were used to create the expansion coefficients), a 10% bandwidth moving filter is implemented and is shown in figure 44, relative to the original function. With this smoother spectral profile, the linear estimation coefficients are improved (not shown).

The cross spectral densities of the near field pressure are shown in figures 45 and 46 where the latter of the two has been transformed from an azimuthal separation  $\Delta\theta = 24^\circ$ , to Fourier-azimuthal modes, using the same principles applied to the velocity field. The results illustrate a shift to higher peak frequencies for higher Fourier-azimuthal mode numbers.

Our formulations for the low-dimensional estimate will not include a cross-spectral tensor with the mathematical sophistication (created in equation 42 and inserted into equation 43) of the near field pressure as a function of mode number. However, from these findings, it may prove to be more advantageous if one chooses to do so. Such an approach would simply relate the velocity field, and the near field pressure, in Fourier-azimuthal mode space.

One underlying limitation does stand out using either approach. If the velocity field is to be broken into a series of Fourier-azimuthal modes, from which the near field pressure becomes the basis of the estimation, then the smallest resolvable mode/structure attainable is limited to the modal (Fourier-azimuthal) resolution of the pressure array. In this study there are  $N = 15$  pressure transducers capable of resolving  $\frac{N}{2} \approx 7$  modes resulting in the smallest resolvable azimuthal event of  $m = 6$ .

The cross spectral densities  $\hat{S}_j(n, m, z_o, f)$  between the *joint* expansion coefficients  $\hat{a}_n(m, z_o, t_s)$  and the near field pressure  $p_j(t_s - \tau)$  are shown in figures 47 to 52 at  $\frac{z}{D} = 3, 5$  and 8, by comparing the first 5 POD modes using individual Fourier-azimuthal modes (of the velocity). For the  $m = 0$  mode, the variation in the amplitude diminishes with increasing distance from the near field pressure. However, for the  $m = 5$  mode, the amplitude differential remains

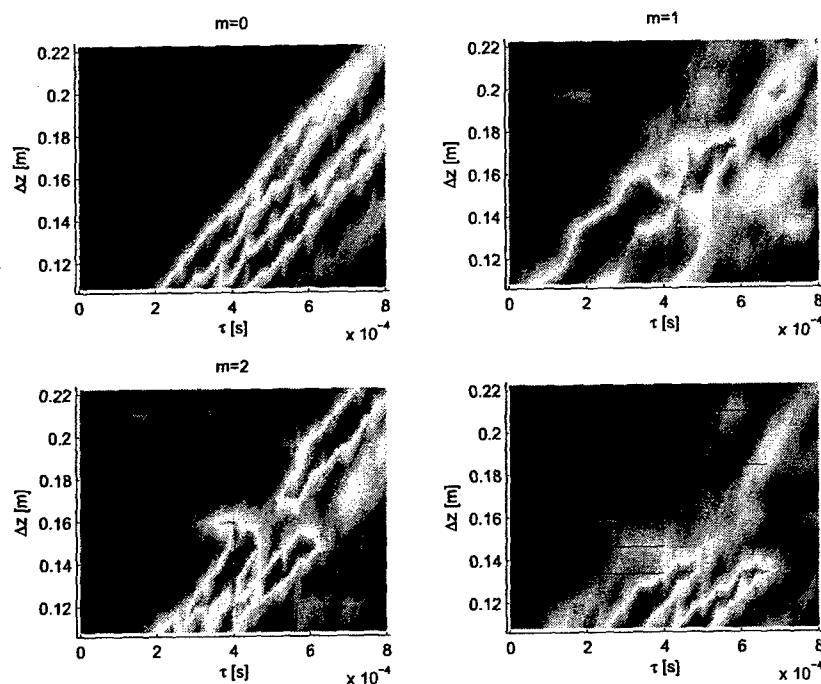


Figure 41. Space time correlation function  $\rho_{\Psi(1,m,\tau)}$  for  $m = 0$  to 3 and  $n = 1$  with near field pressure array using scalar *joint* decomposition, Mach 0.85.

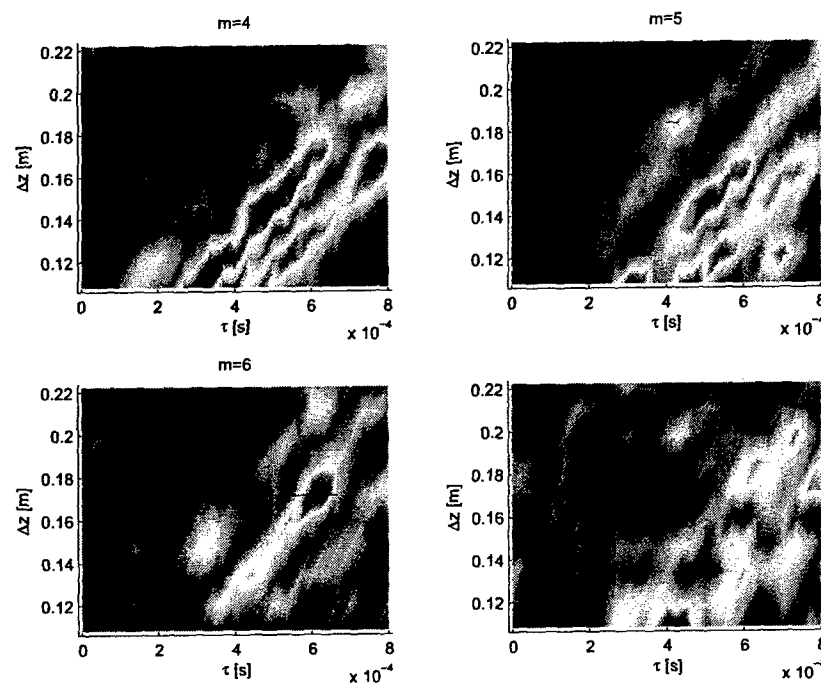


Figure 42. Space time correlation function  $\rho_{\Psi(1,m,\tau)}$  for  $m = 4$  to 7 and  $n = 1$  with near field pressure array using scalar *joint* decomposition, Mach 0.85.

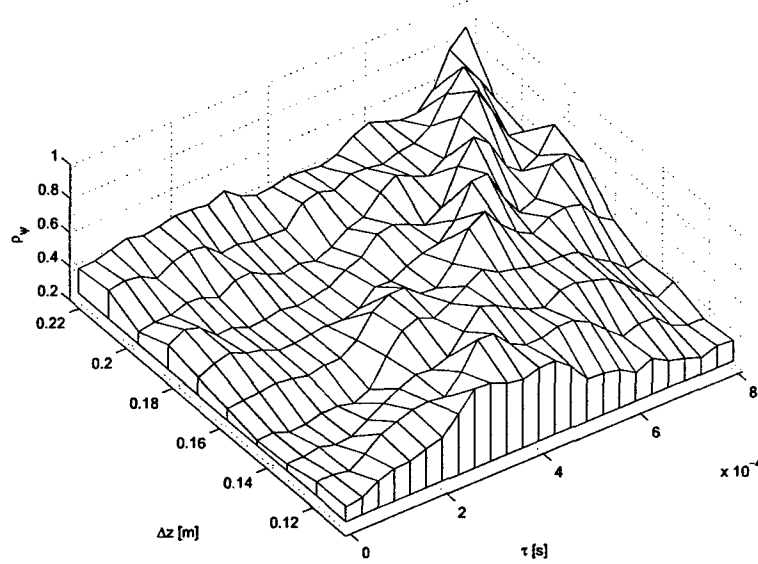


Figure 43. Space time correlation function for  $n = 1$ , averaged over  $m = 0$  to 9, with near field pressure array using scalar *joint* decomposition, Mach 0.85.

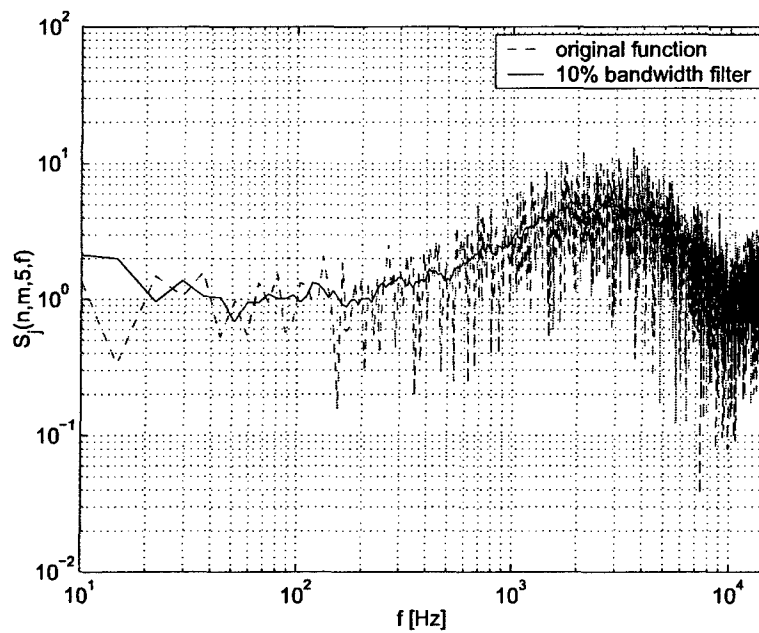


Figure 44. Original cross-spectral density along with a 10% bandwidth moving filter, Mach 0.85.

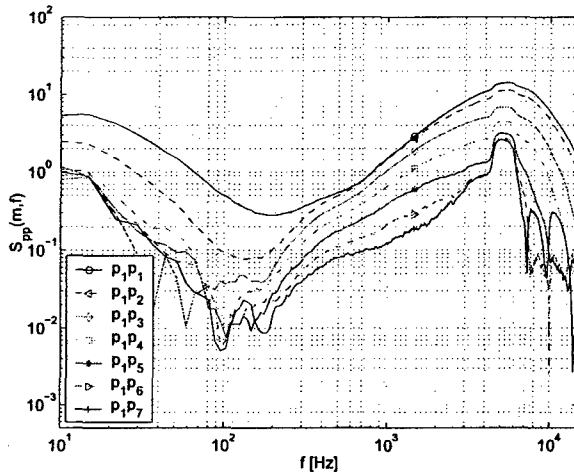


Figure 45. Lip pressure cross spectral density at Mach 0.85,  $f_s = 30 \text{ kHz}$ .

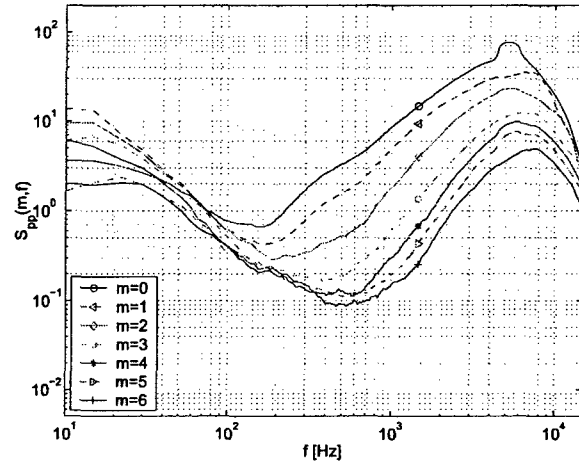


Figure 46. Lip pressure spectral density as a function of azimuthal mode number.

consistently large throughout all regions of the flow. Following the same theme, the cross spectral densities are shown as a function of streamwise position (figures 53 to 56) for the first POD mode, and Fourier-azimuthal modes 0, 2, 5 and 7.

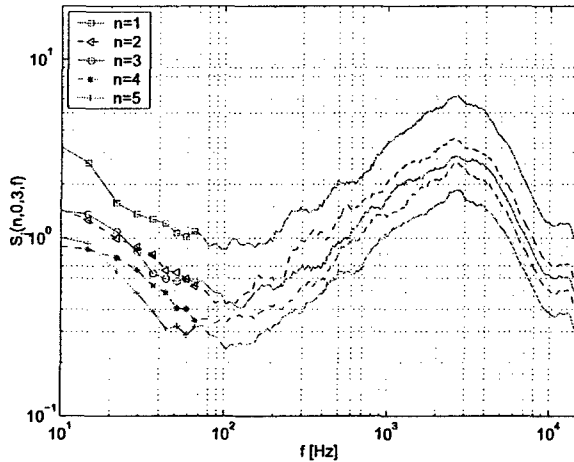


Figure 47. Cross spectral density  $\hat{S}_j(n, 0, 3, f)$  averaged over all transducers.

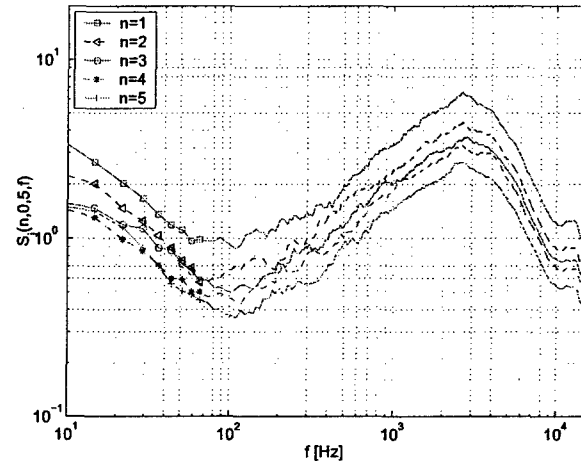


Figure 48. Cross spectral density  $\hat{S}_j(n, 0, 5, f)$  averaged over all transducers.

The decay rate from all of these plots follows that of the near field pressure ( $\approx k^{-6}$ ), and the differential in the spectral amplitude follows that of the eigenvalue distribution presented earlier.

### C. Spectral Characteristics of the Estimate

After solving equation 46 for a low-dimensional estimate of the streamwise  $u$ -component of the fluctuating velocity field, the auto spectral densities are determined. These are plotted in figures 57, 58 and 59 at  $\frac{z}{D} = 3, 5$  and  $8$ , respectively. Each low-dimensional ( $m=0:6$ ) and

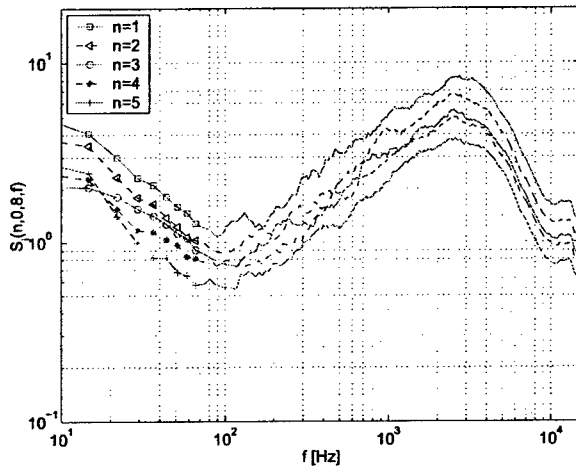


Figure 49. Cross spectral density  $\hat{S}_j(n, 0, 8, f)$  averaged over all transducers.

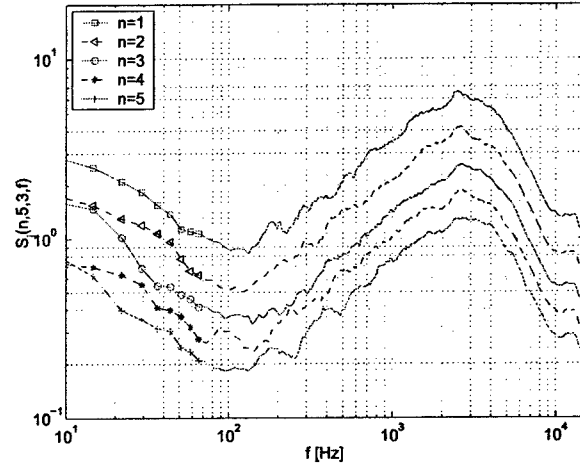


Figure 50. Cross spectral density  $\hat{S}_j(n, 5, 3, f)$  averaged over all transducers.

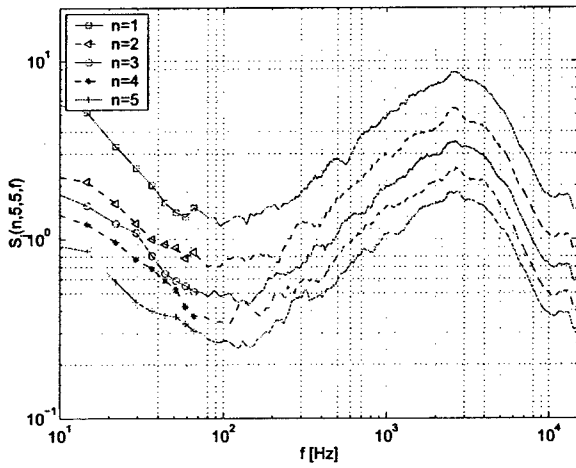


Figure 51. Cross spectral density  $\hat{S}_j(n, 5, 5, f)$  averaged over all transducers.

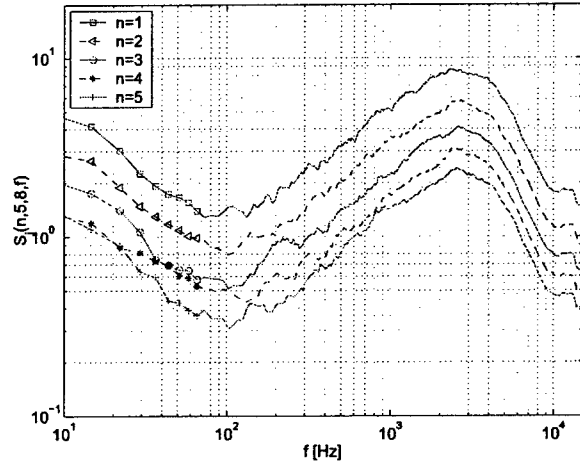


Figure 52. Cross spectral density  $\hat{S}_j(n, 5, 8, f)$  averaged over all transducers.

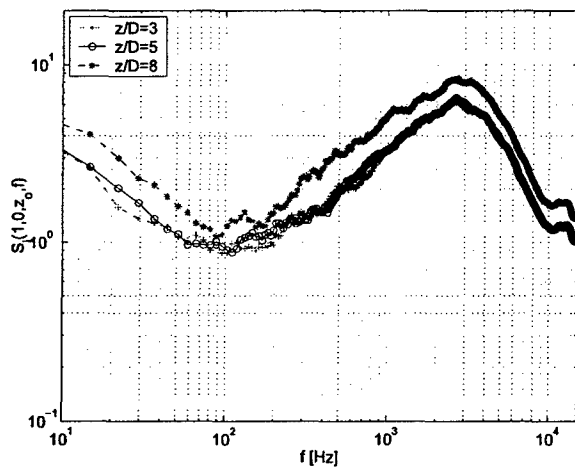


Figure 53. Cross spectral density  $\hat{S}_j(1,0,z_o,f)$  averaged over all transducers.

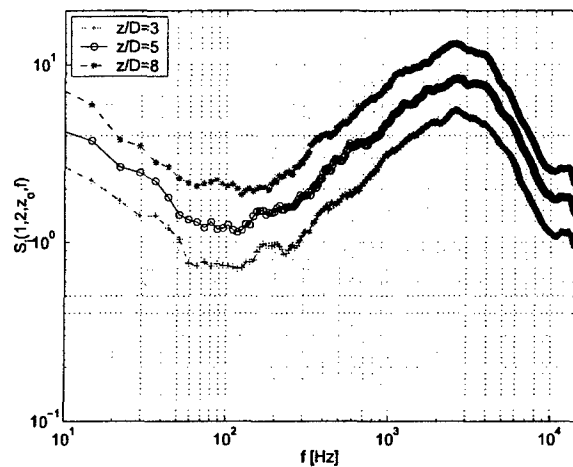


Figure 54. Cross spectral density  $\hat{S}_j(1,2,z_o,f)$  averaged over all transducers.

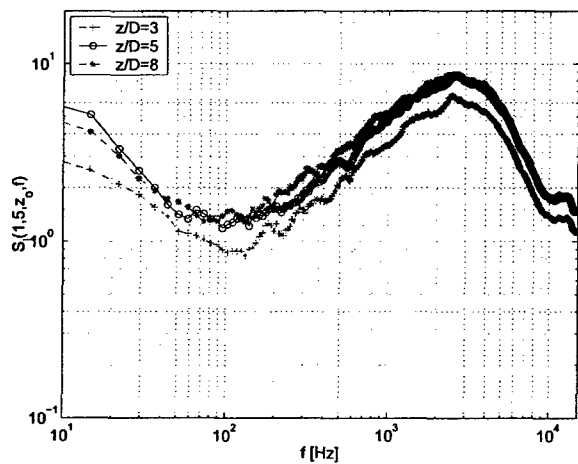


Figure 55. Cross spectral density  $\hat{S}_j(1,5,z_o,f)$  averaged over all transducers.

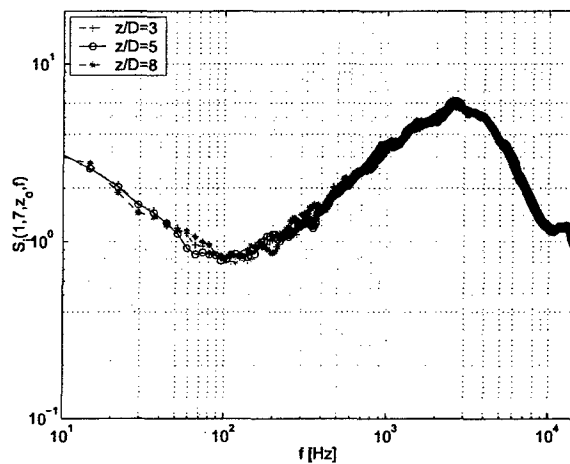


Figure 56. Cross spectral density  $\hat{S}_j(1,7,z_o,f)$  averaged over all transducers.

discrete ( $m=0,3,4$ ) spectral density employs the first POD mode only, and can be thought of as a single-point measurement. These are shown at the center of the jet ( $\frac{r}{R} = 0$ ) where turbulence intensities are the weakest, and at the center of the mixing layer ( $\frac{r}{R} = 1$ ), where turbulence intensities are greatest.

Taylor *et al.*<sup>14</sup> and Ukeiley *et al.*,<sup>63</sup> using cross-wires in NASA Langley's *SAJF*, showed a high degree of similarity in the auto spectral densities of the axisymmetric jet at Mach 0.3, 0.6 and 0.85.

From these figures, we can see that before the collapse of the potential core at  $\frac{z}{D} = 3$ , the center of the jet is completely dominated by the  $m = 0$  mode, whereas the center of the mixing layer is a characterization of all modes ( $m = 0 : 6$ ) included in the low-dimensional estimate. After the collapse of the potential core, the center of the jet is influenced by additional modes, other than  $m = 0$ .

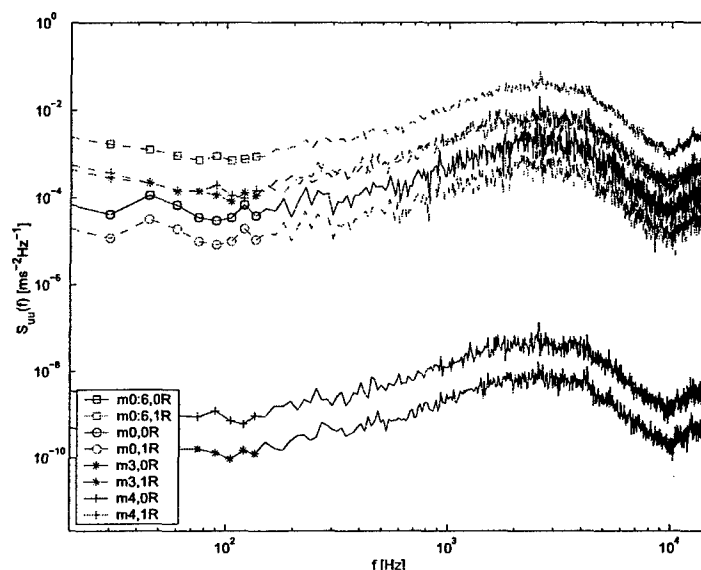


Figure 57. Auto spectral density of streamwise velocity estimate,  $\frac{z}{D} = 3$ .

## VIII. A Time Dependent Estimate of the Low-Dimensional Velocity Field

An estimate of the most energetic events in the sound source regions of the Mach 0.85 jet are shown using the scalar ( $u$ -component only) form of the *joint* decomposition in equation 46. As we illustrated in the previous section, the timescales of the most energetic modes ( $\sim 3kHz$ ) are easily realized because of the high bandwidth capabilities of the unconditional events (the near field pressure is sampled at  $f_s = 30kHz$ ). Also, since the near field pressure has been shown to possess a single spectral characteristic, the linear estimation coefficients from equation 43 are formulated in such a manner as to preserve the natural spectral characteristics of the modal events, using cross spectral information between the conditional and

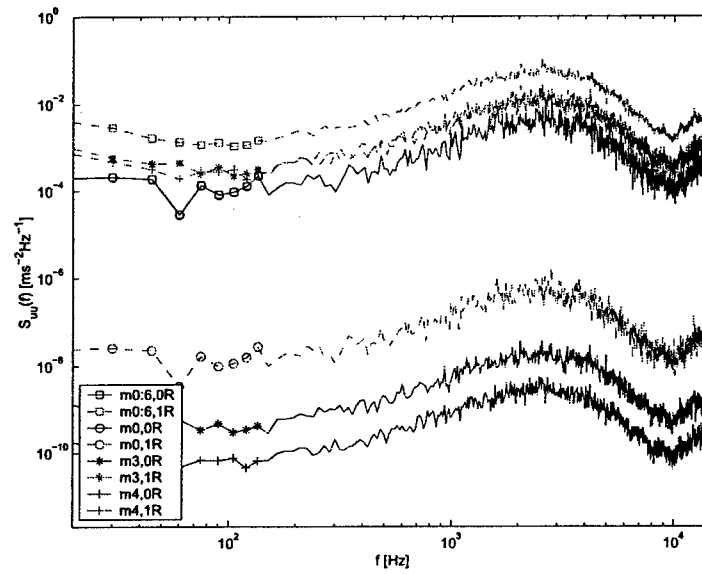


Figure 58. Auto spectral density of streamwise velocity estimate,  $\frac{z}{D} = 5$ .

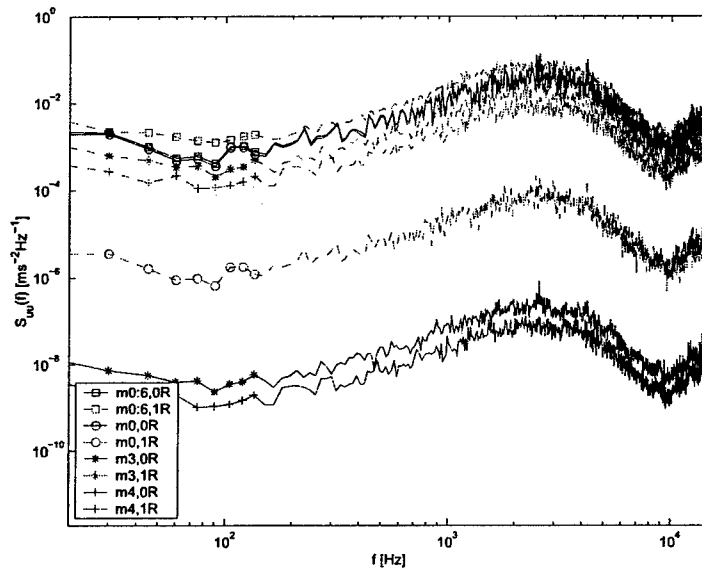


Figure 59. Auto spectral density of streamwise velocity estimate,  $\frac{z}{D} = 8$ .

unconditional events in the estimate.

In figure 60, a reconstruction using the first POD mode and Fourier-azimuthal modes 0 through 6, at an initial time step  $t_o$ , is shown. Two time steps later at  $2\Delta t = 6.7e^{-5}s$  in figure 61, the same events are shown and have evolved.

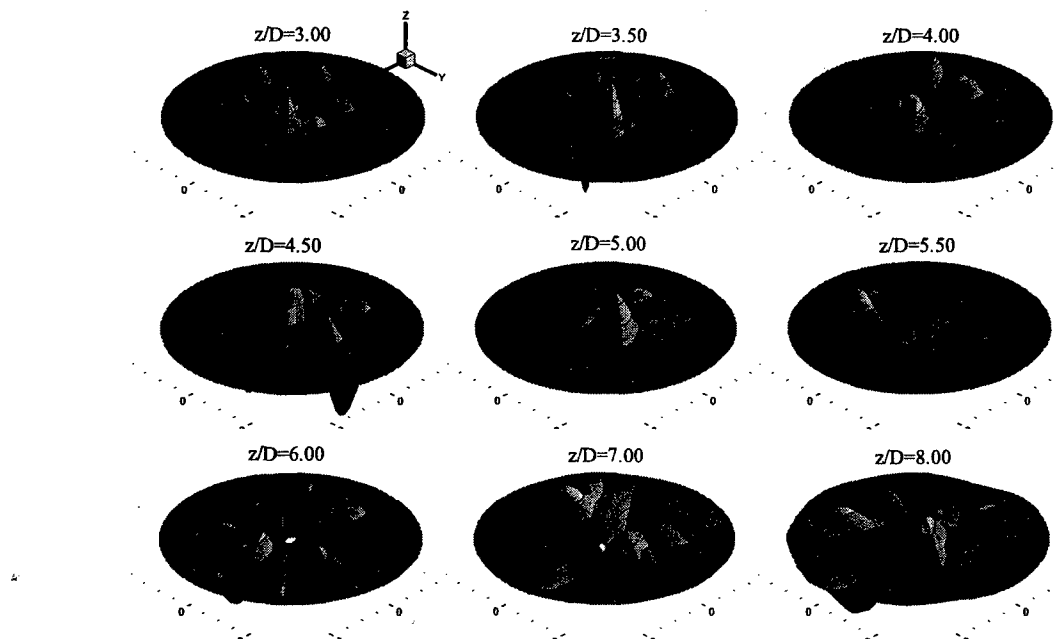
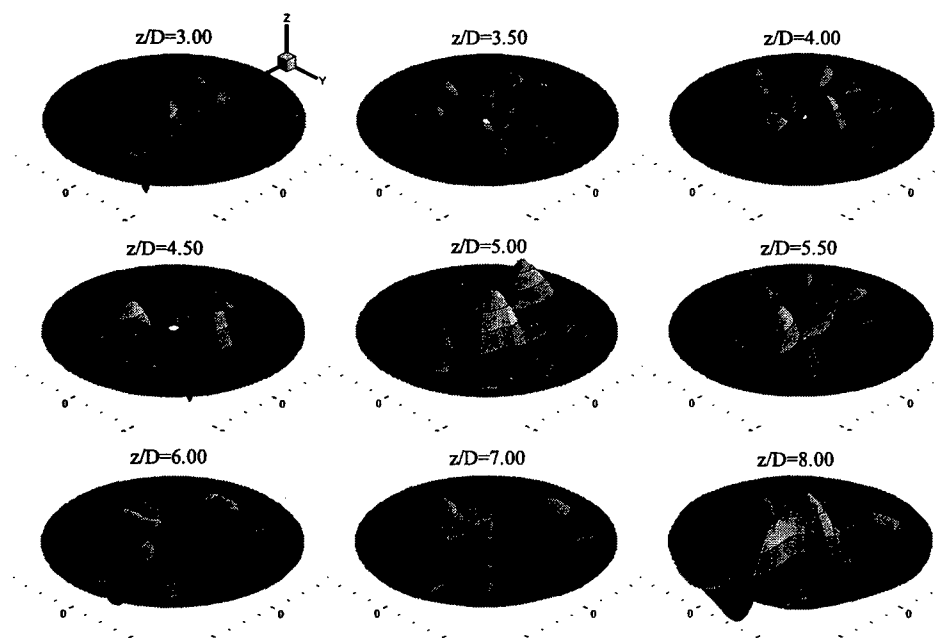


Figure 60. Low dimensional estimate of the streamwise velocity component at  $t_o$  using  $n = 1$  and  $m = 0 : 6$  from near field pressure via *MCT*.

In these figures, we can see that there is a multitude of information in the estimate at  $\frac{z}{D} = 3$ , similar to the original low-dimensional reconstructions shown earlier. As the events convect downstream towards  $8D$ , they are shown to grow azimuthally and radially by shifting energy to lower more energetic modes. Comparing the events at  $4D$  and  $4.5D$  at  $t_o$ , to the events at  $t_o + 2\Delta t$ , the structure in the lower quadrant of the image has rapidly erupted from a single characteristic event to two characteristic events. This small segment of the evolutionary model presented here illustrates an instant when energy is transferred from lower modal events to higher modal events. This instantaneous transfer of energy among the more energetic modes is thought to possess the signature features responsible for much of the local sources of acoustic energy.

### A. Discrete Modal Reconstruction

Previously, we demonstrated our ability to reconstruct any of the Fourier-azimuthal modes individually. By extending this idea to the low-dimensional estimate, we are able to view (phase aligned in time) the evolution of these discrete modes, relative to a superposition of the individual modes. We will choose to do this using an estimate of the velocity field in the most probable sound source region of this flow:  $\frac{z}{D} = 4$ . This time series reconstruction, shown successively in figures 62 to 67, illustrates discrete Fourier-azimuthal modes 0, 3, 4, 5 and 6, with a superposition of Fourier-azimuthal modes  $m = 0 : 6$  located in the top left



**Figure 61.** Low dimensional estimate of the streamwise velocity component at  $t_o + 2\Delta t$  using  $n = 1$  and  $m = 0 : 6$  from near field pressure via MCT.

corner of each figure. At  $t_o$ , the  $m = 0$  is dormant, and the superposition model is a reflection of the energy from all other modes. As time increases, from  $t_o$  to  $+ \Delta t$ , to  $+ 2\Delta t$ , the  $m = 0$  mode erupts, while very little energy presides in the higher modes. As the  $m = 0$  mode decays, the higher modal events increase in energy. Thus, the energy during this process is rapidly transferred from the lower modes to the higher modes.

This evolutionary superposition model resembles the *volcano* like eruption initially modelled by Glauser *et al.*,<sup>38</sup> and later shown (*via* 138 single-wire experiment) by Citriniti & George.<sup>3</sup> In our view, this rapid transfer of energy is the high strain, short duration event, which was postulated by Seiner<sup>13</sup> as the source mechanism for the sound generation in these highly dynamic flows. Our next step is to follow through to see if this is indeed the case by using the simultaneously sampled far field noise data in conjunction with this low dimensional velocity field data.

## References

- <sup>1</sup>ADRIAN R.J. 1977 On the role of conditional averages in turbulence theory. *In Proc. 4th Biennial Symp. on Turbulence in Liquids*.
- <sup>2</sup>BONNET J.-P. COLE D.R. DELVILLE J. GLAUSER M.N. & UKEILEY L.S. 1994 Stochastic estimation and proper orthogonal decomposition: Complementary techniques for identifying structure. *Experiments in Fluids* **84**, 307-314.
- <sup>3</sup>CITRINITI J.H. & GEORGE W.K. 2000 Reconstruction of the global velocity field in the axisymmetric mixing layer utilizing the proper orthogonal decomposition. *J. Fluid Mech.* **418**, 137-166.
- <sup>4</sup>GLAUSER M.N. LEIB S.J. & GEORGE W.K. 1987 Coherent Structures in the Axisymmetric Jet Mixing Layer. *Turbulent Shear Flows 5*, Springer, eds. Durst et al, p. 134.

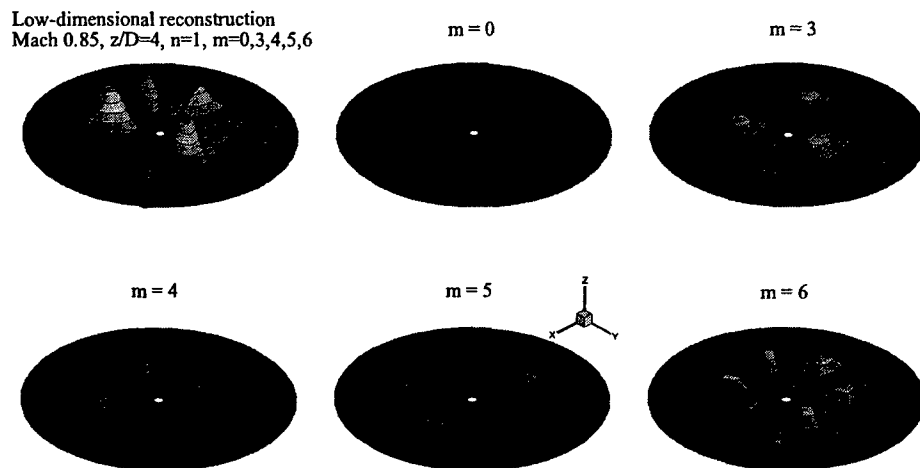


Figure 62. Low dimensional velocity estimate (u-component) at  $t_0$  using  $n = 1$  and  $m = 0 : 6$  and discrete modes ( $m=0,3,4,5,6$ ),  $\frac{z}{D} = 4$ .

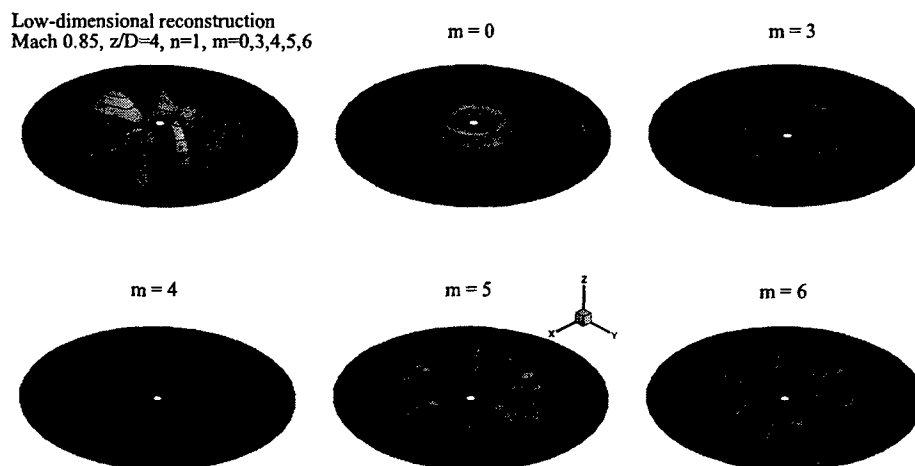


Figure 63. Low dimensional velocity estimate (u-component) at  $t_0 + \Delta t$  using  $n = 1$  and  $m = 0 : 6$  and discrete modes ( $m=0,3,4,5,6$ ),  $\frac{z}{D} = 4$ .

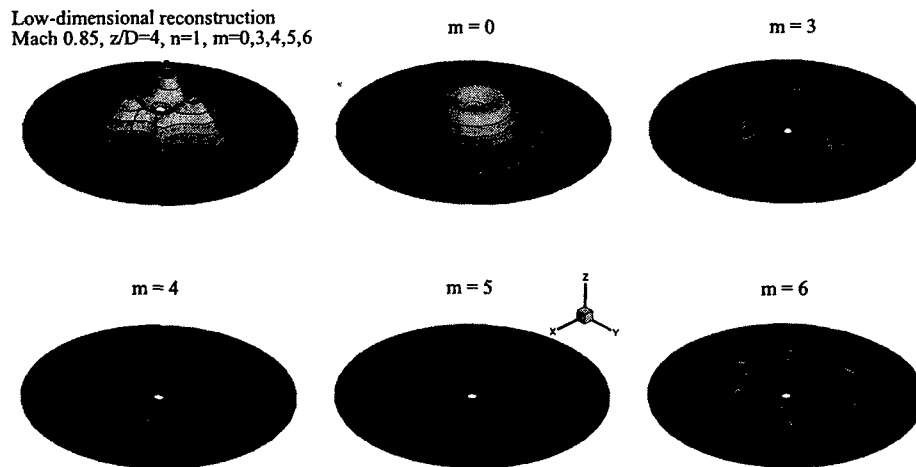


Figure 64. Low dimensional velocity estimate (u-component) at  $t_o + 2\Delta t$  using  $n = 1$  and  $m = 0 : 6$  and discrete modes ( $m=0,3,4,5,6$ ),  $\frac{z}{D} = 4$ .

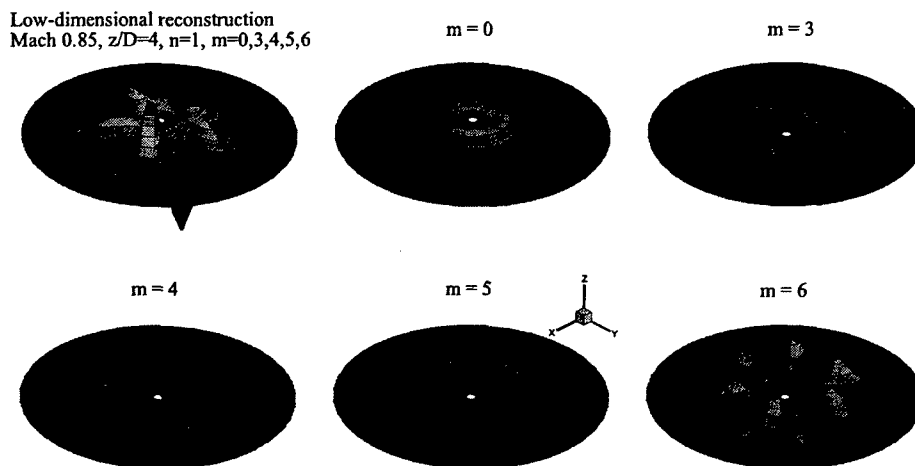


Figure 65. Low dimensional velocity estimate (u-component) at  $t_o + 3\Delta t$  using  $n = 1$  and  $m = 0 : 6$  and discrete modes ( $m=0,3,4,5,6$ ),  $\frac{z}{D} = 4$ .

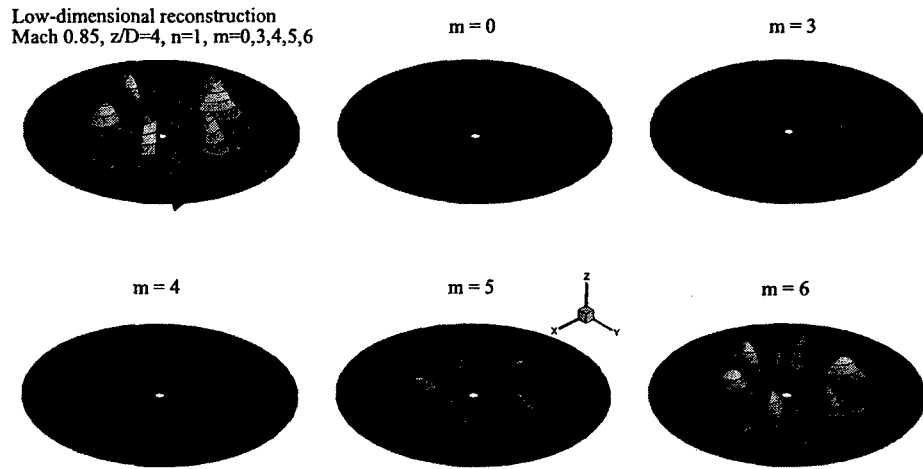


Figure 66. Low dimensional velocity estimate (u-component) at  $t_o + 4\Delta t$  using  $n = 1$  and  $m = 0 : 6$  and discrete modes ( $m=0,3,4,5,6$ ),  $\frac{z}{D} = 4$ .

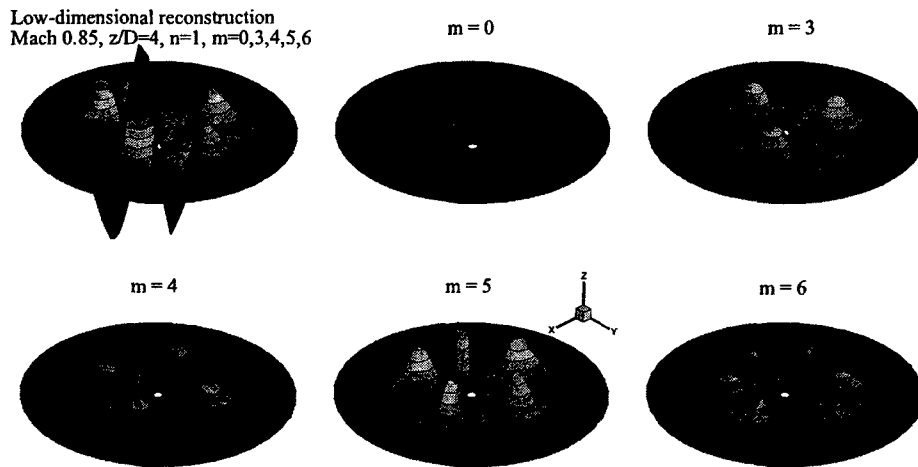


Figure 67. Low dimensional velocity estimate (u-component) at  $t_o + 5\Delta t$  using  $n = 1$  and  $m = 0 : 6$  and discrete modes ( $m=0,3,4,5,6$ ),  $\frac{z}{D} = 4$ .

- <sup>5</sup>GLAUSER M.N. & GEORGE W.K. 1992 Application of multipoint measurements for flow characterization. *Experimental and Thermal Fluid Sciences*, pp 617-632.
- <sup>6</sup>GLAUSER M.N. YOUNG M.J. HIGUCHI H. TINNEY C.E. & CARLSON H. 2004 POD based experimental flow control on a NACA-4412 airfoil 42<sup>nd</sup> AIAA Aerospace Sciences Meeting and Exhibit, (Invited) Reno, NV 2004-0575.
- <sup>7</sup>HALL A.M. TINNEY C.E. & GLAUSER M.N. 2005 Investigatgin the 'modified' Complementary Technique Using Pressure-Velocity Correlations of an Axisymmetric Jet 43<sup>rd</sup> AIAA Aerospace Sciences Meeting and Exhibit, Reno, NV 2005-0039.
- <sup>8</sup>JUNG D. GAMARD S. & GEORGE W.K. 2004 Downstream evolution of the most energetic modes in a turbulent axisymmetric jet at high Reynolds number. Part 1. The near-field region. *to appear in J. Fluid Mech.*, 1-32.
- <sup>9</sup>LUMLEY J.L. 1967 The structure of inhomogeneous turbulent flows. *Atmospheric Turbulence and Radio Wave Propagation*, Eds. Yaglom and Tatarsky, Nauka, Moscow.
- <sup>10</sup>MOLLO-CHRISTENSEN E. KOLPIN M.A. & MARTUCCELLI J.R. 1963 Experiments on jet flows and jet noise far-field spectra and directivity patterns. *J. Fluid Mech.* **18**, 285-301.
- <sup>11</sup>MURRAY N. & UKEILEY L.S. 2003 Estimation of the flow field from surface pressure measurements in an open cavity. *AIAA Journal*, **41**:5, pp. 969-972.
- <sup>12</sup>NAGUIB A.M. WARK C.E. & JUCKENHÖFEL O. 2001 Stochastic estimation and flow sources associated with surface pressure events in a turbulent boundary layer. *Physics of Fluids* **13**:9, 2611-2626.
- <sup>13</sup>SEINER J. 1998 A New Rational Approach to Jet Noise Reduction. *Theoretical and Computational Fluid Dynamics*, **10**, pp. 373-383.
- <sup>14</sup>TAYLOR J.A. UKEILEY L.S. & GLAUSER M.N. 2001 A low-dimensional description of the compressible axisymmetric shear layer. 39<sup>th</sup> AIAA Aerospace Sciences Meeting and Exhibit, Reno, NV 2001-0292.
- <sup>15</sup>TAYLOR J. A. & GLAUSER M. N. 2002 Towards Practical Flow Sensing and Control via POD and LSE Based Low-Dimensional Tools. 2002 ASME Fluids Engineering Division Summer Meeting, Montreal, ASME Paper FEDSM2002-31416. To appear, J. Fluids Eng. March 2004.
- <sup>16</sup>TINNEY C.E. HALL A. GLAUSER M.N. UKEILEY L.S. & COUGHLIN T. 2004 Designing an anechoic chamber for the experimental study of high speed heated jets. 42<sup>nd</sup> AIAA Aerospace Sciences Meeting and Exhibit, Reno, NV 2004-0010.
- <sup>17</sup>TINNEY C.E. EATON E. TAYLOR J.A. & GLAUSER M.N. Low dimensional azimuthal characteristics of suddenly expanding axisymmetric flows, part 1: proper orthogonal decomposition. under consideration in *J. Fluid Mech.*, submitted 2004.
- <sup>18</sup>UKEILEY L. SEINER J. & PONTON M. 1999 Azimuthal structure of an axisymmetric jet mixing layer. ASME Paper FEDSM99-7252.
- <sup>19</sup>UKEILEY L. S. 2003 Examination of Quadrupole Sources in a Transonic Jet. 38<sup>th</sup> AIAA Aerospace Sciences Meeting and Exhibit, Reno, NV 2003-0084.
- <sup>20</sup>UKEILEY L. MANN R. TINNEY C.E. & GLAUSER M.N. 2004 Spatial Correlations in a Transonic Jet. 34<sup>th</sup> AIAA Fluid Dynamics Conference, Portland, Oregon, AIAA2004-2654, June 2004.
- <sup>21</sup>Adrian, R. (1979) "Conditional Eddied in Isotropic Turbulence," *Phys. of Fluids*, **22**(11), pp. 2065-2070.
- <sup>22</sup>Adrian, R. and Moin, P. (1988) "Stochastic Estimation of Organized Turbulent Structure: Homogeneous Shear Flow," *Journal of Fluid Mechanics*, **190**(11), pp. 531-559.
- <sup>23</sup>Adrian, R., Jones, R., Chung, M. Hassan, Y., Nithiannada, C. and Tung T. (1989) "Approximation of Turbulent Conditional Averages by Stochastic Estimation," *Phys. of Fluids*, **1**(6), pp. 992-998.
- <sup>24</sup>Ahuja, K. K. (2003) "Designing Clean Jet Noise Facilities and Making Accurate Jet Noise Measurements." AIAA 2003-0706, 1-34.
- <sup>25</sup>Avital, E. J., Sandham, N. M., Lou, K. H and Musafir, R. E. (1999) "Calculation of Basic Sound Radiation of Axisymmetric Jets by Direct Numerical Simulation," *AIAA Journal*, **37**(2), pp. 161-168.
- <sup>26</sup>Aubry, N., Holmes, P., Lumley, J. and Stone, E. (1988) "The Dynamics of Coherent Structures in the Wall Region of a Turbulent Boundary Layer," *J. Fluid Mech.*, **192**, pp. 115-173.
- <sup>27</sup>Bastin, F., Lafon, P., Candel, S. (1997) "Computation of jet mixing noise due to coherent structures: the plane case." *J. Fluid Mech.*, **335**, pp. 261-304.

- <sup>28</sup>Berkooz, G., Holmes, P. and Lumley, J. (1993) "The Proper Orthogonal Decomposition in the Analysis of Turbulent Flows", *Annual Review of Fluid Mechanics*, **25**, pp. 539-575.
- <sup>29</sup>Bernal, L. and Roshko, A. (1986) "Streamwise Vortex Structure in Plane Mixing Layers," *Journal of Fluid Mechanics*, **170**, pp. 499-525.
- <sup>30</sup>Brown, G. L. & Roshko, A. (1974) "Density effects and large structures in turbulent mixing layers." *J. Fluid Mech.* **64**:4, 775-816.
- <sup>31</sup>Cole, D.R., Glauser, M.N. and Guezennec, Y.G., (1991), "An Application of Stochastic Estimation to the Jet Mixing Layer," *Physics of Fluids A*, **4**(1).
- <sup>32</sup>Creighton, D. G. (1975) "Basic Principles of Aerodynamic Noise Generation," *Proc. Aerospace Sci.* **16**(1), pp. 31-96.
- <sup>33</sup>Delville, J., Ukeiley, L., Cordier, L., Bonnet, J. P. & Glauser, M. N. (1999) "Examination of large scale structures in a turbulent plane mixing layer. Part 1: Proper Orthogonal Decomposition." *J. Fluid Mech.* **391**, 91-122.
- <sup>34</sup>Dosanjh, D. S., Bhutiani, P. K., Ahuja, K. K., (1977) "Supersonic Jet Noise Suppression by Coaxial Multi-Nozzle Cold/Heated Jet Flows." Department of Transportation Final Report, Washington DC.
- <sup>35</sup>Ffowcs Williams, L. E., Kempton, A. J. (1978) "The noise from the large scale structure of a jet." *J. Fluid Mech.* **84**, 673-694.
- <sup>36</sup>Freund, J. B. (2001) "Noise sources in a low-Reynolds-number turbulent jet at Mach 0.9." *J. Fluid Mech.* **438**, 277-305.
- <sup>37</sup>Gamard, S., George, W. K., Jung, D. & Woodward, S. (2002) "Application of a "slice" proper orthogonal decomposition to the far field of an axisymmetric turbulent jet." *Physics of Fluids* **14** (6)
- <sup>38</sup>Glauser, M. and George, W. K. (1987) "An Orthogonal Decomposition of the Axisymmetric Jet Mixing Layer Utilizing Cross-Wire Measurements," *Proceedings of the 6th Symposium on Turbulent Shear Flows*.
- <sup>39</sup>Goldstein, M. E. (1976) *Aeroacoustics*, McGraw-Hill.
- <sup>40</sup>Gordeyev, S.V., & Thomas, F. O. (2000) "Coherent Structure and the Turbulent Planar Jet. Part 1. Extraction of Proper Orthogonal Decomposition Eigenmodes and Their Self-Similarity." *J. Fluid Mech.* **414**, 145-194
- <sup>41</sup>Grinstein, F., Glauser, M. and George, W. K. (1995) "Vorticity in Jets," *Fluid Vortices*, edited by S. Green, pp. 65-94.
- <sup>42</sup>Hileman, J., Thurow, B. and Samimy, M. (2001) "Determination of Noise Sources Within a High-Speed Jet Via Simultaneous Acoustic Measurements and Real-Time Flow Visualization," AIAA Paper 2001-0374.
- <sup>43</sup>Holmes, P., Lumley, J. and Berkooz, G. (1996) *Turbulence, Coherent Structures, Dynamical Systems and Symmetry*, Cambridge University Press.
- <sup>44</sup>Hussain, A. K. M. F. (1983) "Coherent Structures Reality and Myth," *Physics of Fluids A*, **26**, pp. 2816-2850.
- <sup>45</sup>Hussain, A. K. M. F. (1986) "Coherent Structures and Turbulence," *J. Fluid Mech.*, **173**, pp. 303.
- <sup>46</sup>Jansson, D., Mathew, J., Hubner, J., Sheplak, M., Cattafesta, L. (2002) "Design and Validation of an Aeroacoustic Anechoic Test Facility." AIAA 2002-2466, 1-10.
- <sup>47</sup>Juve, D., Sunyach, M. and Comte-Bellot, G. (1980) "Intermittency of the Noise Emission in Subsonic Cold Jets," *Journal of Sound and Vibration* **71**(3), pp. 319-332.
- <sup>48</sup>Lighthill, M. J. (1952) "On Sound Generated Aerodynamically: General Theory," *Proceedings of the Royal Society* **211**(1106), pp. 564-587.
- <sup>49</sup>Lighthill, M. J. (1954) "On Sound Generated Aerodynamically: II Turbulence as a Source of Sound," *Proceedings of the Royal Society* **222**(1148), pp. 1-32.
- <sup>50</sup>Lilley G. M. (1991) "Jet Noise Classical Theory and Experiments," *Aeroacoustics of Flight Vehicles: Theory and Practice*, NASA Reference Publication 1258.
- <sup>51</sup>Liu, J. (1989) "Coherent Structures in Transitional and Turbulent Free Shear Flows," *Annual Review of Fluid Mechanics*, **21**, pp. 285.
- <sup>52</sup>Lumley, J. L. (1970) *Stochastic Tools in Turbulence*, Academic Press.
- <sup>53</sup>Moin, P., Adrian, R. and Kim, J. (1987) "Stochastic Estimation of Organized Structure in Turbulent Channel Flow," *Proceedings of the 6th Symposium on Turbulent Shear Flows*.

- <sup>54</sup>Moin, P. & Moser, R. D. (1989) "Characteristic eddy decomposition of turbulence in a channel." *J. Fluid Mech.*, **200**, 471-509
- <sup>55</sup>Ponton, M. K., Seiner, J., Ukeiley, L., Jansen, B. (2001) "A new Anechoic Chamber Design for Testing High Temperature Jet Flows." AIAA 2001-2190, 1-8.
- <sup>56</sup>Powell, A. (1998) "Aerodynamic and Jet Noise," *Handbook of Acoustics*, John Wiley & Sons, Inc.
- <sup>57</sup>Schaffar, M. (1979) "Direct Measurements of the Correlation Between Axial In-Jet Velocity Fluctuations and Far Field Noise Near the Axis of a Cold Jet," *Journal of Sound and Vibration*, **64**(1). pp.73-83.
- <sup>58</sup>Seiner, J. M and Reethof, G. (1974) "On the Distribution of Source Coherency in Subsonic Jets," AIAA Paper 74-4.
- <sup>59</sup>Sheplak, M. and Spina, E.F. (1994) "Control of High-Speed Impinging Jet Resonance," AIAA Journal, **32**, pp. 1583-1588.
- <sup>60</sup>Tam, C. K. W. (1998) "Jet Noise: Since 1952," *Theoretical and Computational Fluid Dynamics*, **10**, pp 393-405.
- <sup>61</sup>Townsend, A. A. (1956) "The structure of turbulent shear flow.", 2<sup>nd</sup> edn. *Cambridge University Press*, Cambridge, UK.
- <sup>62</sup>Tung, T.C. and Adrian, R.J. (1980) "Higher-Order Estimates of Conditional Eddies in Isotropic Turbulence," *Phys. Fluids* **23**, 1469.
- <sup>63</sup>Ukeiley, L. and Seiner, J. (1998) "Examination of Large Scale Structures in a Transonic Jet Mixing Layer," ASME FEDSM98-5234.
- <sup>64</sup>Ukeiley, L., Cordier, L., Manceau, R., Delville, J., Glauser, M. N. & Bonnet, J. P. (2001) "Examination of large scale structures in a turbulent plane mixing layer. Part 2: Dynamical Systems Model." *J. Fluid Mech.*, **441**, 67-108.
- <sup>65</sup>Winant, C. D. & Browand, F. K. (1974) "Vortex pairing: the mechanism of turbulent mixing layer growth at moderate Reynolds numbers." *J. Fluid Mech.* **63**, 237.
- <sup>66</sup>Wlezien, R. W., Horner, G. C., McGowan, A. R., Padula, S. L., Scott, M. A., Silcox, R. J. and Simpson, J. O. (1998) "The Aircraft Morphing Program," AIAA Paper 98-1927.
- <sup>67</sup>Zheng, X. (1991) "A Low Dimensional Dynamical Systems Description of Coherent Structures in the Axisymmetric Jet Mixing Layer," Ph.D. Thesis Clarkson University.

MA AFRL-SR-AR-TR-05-

## REPORT DOCUMENTATION PAGE

0192

Public reporting burden for this collection of information is estimated to average 1 hour per response, including the time for reviewing instructions, searching existing data sources, gathering the required data, completing and reviewing this collection of information. Send comments regarding this burden estimate or any other aspect of this collection of information, including suggestions for reducing this burden to Department of Defense, Washington Headquarters Services, Directorate for Information Operations and Reports (0704-0188), 1215 Jefferson Davis Highway, Suite 1204, Arlington, VA 22202-4302. Respondents should be aware that notwithstanding any other provision of law, no person shall be subject to any penalty for failing to comply with a collection of information if it does not display a currently valid OMB control number. PLEASE DO NOT RETURN YOUR FORM TO THE ABOVE ADDRESS.

1. REPORT DATE (DD-MM-YYYY) 02/14/2005		2. REPORT TYPE Final Technical		3. DATES COVERED (From - To) January 2002 - Nov 2004	
4. TITLE AND SUBTITLE Low Dimensional Methods for Jet Noise Control				5a. CONTRACT NUMBER	
				5b. GRANT NUMBER F49620-02-1-0087	
				5c. PROGRAM ELEMENT NUMBER	
6. AUTHOR(S) Charles Tinney, Mark Glauser and Larry Ukeiley				5d. PROJECT NUMBER	
				5e. TASK NUMBER	
				5f. WORK UNIT NUMBER	
7. PERFORMING ORGANIZATION NAME(S) AND ADDRESS(ES) Syracuse University Department of Mechanical and Aerospace Engineering Syracuse, NY 13244 University of Mississippi Jamie Whitten National Center for Physical Acoustics University, Mississippi, 38677				8. PERFORMING ORGANIZATION REPORT NUMBER	
9. SPONSORING / MONITORING AGENCY NAME(S) AND ADDRESS(ES) Dr. John Schmisser AFOSR/NA 4015 Wilson Boulevard Room 713 Arlington, VA 22203-1954				10. SPONSOR/MONITOR'S ACRONYM(S) AFOSR	
				11. SPONSOR/MONITOR'S REPORT NUMBER(S) F49620-02-1-0087	
12. DISTRIBUTION / AVAILABILITY STATEMENT Approved for public release; distribution unlimited.					
13. SUPPLEMENTARY NOTES					
14. ABSTRACT Low-dimensional techniques (i.e., POD, Linear Stochastic Estimation) are applied to the compressible jet mixing layer in the sound source regions of the flow. Measurements are acquired along the streamwise cross plane using a multi-component PIV system. The low-dimensional analysis is employed to reconstruct temporally, the 3D velocity field, estimated from an azimuthal array of fifteen dynamic pressure transducers positioned near the jet lip. These transducers are located outside of the turbulent sound source regions of the flow, so that the acoustical characteristics of the sound source events are not disturbed. A volcano like event is found similar to the one modeled by Glauser and George, and later confirmed experimentally by Citrinit and George. It is this event that is thought to produce much of the noise experienced in the far field acoustic regions. A survey of the far field noise was performed simultaneously with the near field pressure. Currently we are comparing estimates of the far field noise with those computed from the velocity field extracted in this study.					
15. SUBJECT TERMS High Speed Jets, Noise and Flow Control, Proper Orthogonal Decomposition, Stochastic Estimation					
16. SECURITY CLASSIFICATION OF:			17. LIMITATION OF ABSTRACT UU	18. NUMBER OF PAGES	19a. NAME OF RESPONSIBLE PERSON
a. REPORT UNCLASSIFIED	b. ABSTRACT UNCLASSIFIED	c. THIS PAGE UNCLASSIFIED			19b. TELEPHONE NUMBER (include area code)